Thesis for the Degree of Doctor of Philosophy

Integrated Nonlinear Optics in Silicon Nitride Waveguides

Clemens Krückel

Photonics Laboratory
Department of Microtechnology and Nanoscience (MC2)
Chalmers University of Technology
Göteborg, Sweden, 2017

Integrated Nonlinear Optics in Silicon Nitride Waveguides

Clemens Krückel

Göteborg, May 2017

ISBN 978-91-7597-554-2

Doktorsavhandlingar vid Chalmers Tekniska Högskola
Ny serie 4235
ISSN 0346-718X

Technical Report MC2-356
ISSN 1652-0769

Photonics Laboratory
Department of Microtechnology and Nanoscience (MC2)
Chalmers University of Technology, SE-412 96 Göteborg, Sweden
Phone: +46 (0) 31 772 1000

Front cover illustration: From top left to bottom right. SEM image of a silicon nitride strip waveguide after dry-etching (width 1.65 µm, height 0.7 µm). Optical spectrum of the four-wave mixing process. Simulation of the optical power distribution in a silicon nitride strip waveguide.

Printed by Chalmers reproservice, Chalmers University of Technology
Göteborg, Sweden, May, 2017

Errata

Integrated Nonlinear Optics in Silicon Nitride Waveguides

Clemens Krückel

- Page 12: mismatch of the propagation constant for pump, signal and idler wave is given by $\Delta\beta = \beta_{\mathrm{S}} + \beta_{\mathrm{I}} - 2\beta_{\mathrm{P}}$
- Appendix A: PECVD deposition of silicon dioxide - RF Generator power 60 W
- Appendix A: Spin photoresist S1813 - 4 000 rpm
- Appendix A: Hardbake in oven, photoresist UV60-0.75 - 120°C, 15 min

Integrated Nonlinear Optics in Silicon Nitride Waveguides

Clemens Krückel

Chalmers University of Technology
Department of Microtechnology and Nanoscience (MC2)
Photonics Laboratory, SE-412 96 Göteborg, Sweden

Abstract

Current nanofabrication techniques allow patterning of optical waveguides with submicron cores. This results in strong confinement of light, which leads to high optical intensities. If the waveguides are fabricated with materials that display a large nonlinear Kerr coefficient, then nonlinear optical phenomena can take place in a very efficient manner.
Silicon nitride is a very well-studied material in the electronics industry. The material has a large transparency window, from the ultraviolet to the short-wave infrared, and its fabrication is completely compatible with standard techniques formerly developed by the semiconductor industry. Silicon nitride strip waveguides can also confine light, and diverse applications based on nonlinear optics have been demonstrated before. However, these applications required core thickness above 300 nm and they are very challenging to fabricate in a reliable manner with standard deposition techniques.
In this thesis, we have studied unconventional silicon nitride waveguides that are more robust for fabrication. The first layout corresponds to a thin strip waveguide with low optical confinement and propagation losses of only 6 dB/m. This technology was originally developed at the University of California, Santa Barbara. We used the technology to demonstrate wavelength conversion of high-speed data. In this thesis, we developed another silicon nitride technology that allowed for high light confinement. We discovered that by modifying the stoichiometry of the film during the deposition process, one could drastically change the optical and mechanical properties of the material. With this technology we demonstrated octave-spanning supercontinuum generation in collaboration with the Technical University of Denmark and XPM-based all-optical processing in collaboration with McGill University. These results indicate that this platform is very suitable for nonlinear integrated optics.
The long-term goal of our research is being able to attain an optical parametric amplifier on chip using a continuous-wave pump laser source. In this thesis we benchmarked the losses of high-confinement waveguides for the realization of 10 dB parametric net-gain on chip and identified silicon nitride as the most plausible technology to achieve this goal in the near future.

Keywords: four-wave mixing, integrated optics devices, nanostructure fabrication, nonlinear optical signal processing, nonlinear optics materials, wavelength conversion devices

List of papers

This thesis is based on the following appended papers:

[A] **C. J. Krückel**, V. Torres-Company, P. A. Andrekson, D. T. Spencer, J. F. Bauters, M. J. R. Heck, and J. E. Bowers, "Continuous wave-pumped wavelength conversion in low-loss silicon nitride waveguides," *Optics Letters*, vol. 40, no. 6, pp. 875−878, March 2015.

[B] **C. J. Krückel**, A. Fülöp, T. Klintberg, J. Bengtsson, P. A. Andrekson, and V. Torres-Company, "Linear and nonlinear characterization of low-stress high-confinement silicon-rich nitride waveguides," *Optics Express*, vol. 23, no. 20, pp. 25828−25837, Sept. 2015 + Erratum *Optics Express*, vol. 25, no. 7, pp. 7443−7444, April 2017.

[C] X. Liu, M. Pu, B. Zhou, **C. J. Krückel**, A. Fülöp, V. Torres-Company, and M. Bache, "Octave-spanning supercontinuum generation in a silicon-rich nitride waveguide," *Optics Letters*, vol. 41, no. 12, pp. 2719−2722, June 2016.

[D] M. Rezagholipour Dizaji, **C. J. Krückel**, A. Fülöp, P. A. Andrekson, V. Torres-Company, and L. R. Chen, "Cross-phase-modulation-based wavelength conversion in low-stress silicon-rich nitride waveguide," *Optical Fiber Communication Conference (OFC)*, Anaheim, USA, paper Tu2K.4, March 2016.

[E] M. Rezagholipour Dizaji, **C. J. Krückel**, P. A. Andrekson, V. Torres-Company, and L. R. Chen, "All-optical radio frequency spectrum analyzer based on cross-phase modulation in a silicon-rich nitride waveguide," *IEEE International Topical Meeting on Microwave Photonics (MWP)*, Long Beach, USA, paper ThM1.5, Nov. 2016.

[F] **C. J. Krückel**, A. Fülöp, Z. Ye, P. A. Andrekson, and V. Torres-Company, "Optical bandgap engineering in nonlinear silicon nitride waveguides," Submitted, March 2017.

[G] **C. J. Krückel**, P. A. Andrekson, and V. Torres-Company, "Towards on-chip net-gain in CMOS-compatible waveguides," Accepted to the *Conference on Lasers and Electro-Optics (CLEO) Europe*, Munich, Germany, paper CD-P.14, June 2017.

Related publications and conference contributions by the author not included in the thesis:

Journal papers

[H] A. Fülöp, **C. J. Krückel**, D. Castelló Lurbe, E. Silvestre, and V. Torres-Company, "Triply resonant coherent four-wave mixing in silicon nitride microresonators," *Optics Letters*, vol. 40, no. 17, pp. 4006−4009, March 2015.

Conference presentations and papers

[I] **C. J. Krückel**, V. Torres-Company, P. A. Andrekson, J. Bovington, J. Bauters, M. Heck, and J. Bowers, "Continuous-wave nonlinear optics in low-stress silicon-rich nitride waveguides," *Conference on Lasers and Electro-Optics (CLEO)*, San Jose, USA, paper SW3M.4, June 2014.

[J] **C. J. Krückel**, A. Fülöp, P. A. Andrekson, and V. Torres-Company, "Continuous-wave nonlinear optics in low-stress silicon-rich nitride waveguides," *Optical Fiber Communication Conference (OFC)*, Los Angeles, USA, paper W1K.4, March 2015.

[K] A. Fülöp, **C. J. Krückel**, D. Castelló Lurbe, E. Silvestre, and V. Torres-Company, "Phase-sensitive resonant four-wave mixing in silicon nitride microresonators," *Conference on Lasers and Electro-Optics (CLEO) Europe*, Munich, Germany, paper CD_P_9, June 2015.

[L] **C. J. Krückel**, A. Fülöp, P. A. Andrekson, and V. Torres-Company, "Bandgap engineering in nonlinear silicon nitride waveguides," *Optical Fiber Communication Conference (OFC)*, Los Angeles, USA, paper M3F.6, March 2017.

Acknowledgement

I would like to thank Prof. Peter Andrekson for giving me the opportunity to gain experience and improve my professional skills in the research environment in the photonics laboratory. I acknowledge Prof. Magnus Karlsson for sharing his expertise and answering questions about nonlinear optics.
I want to thank my supervisor Dr. Victor Torres-Company for being a thorough and talented leader.
I would like to thank Prof. John Bowers, Dr. Jared Bauters, Dr. Martijn Heck and Dr. Daryl Spencer from the University of California Santa Barbara for the collaboration and for providing waveguide samples. I also thank Dr. Morten Bache from DTU as well as Mohammad Dizaji and Dr. Lawrence Chen from the McGill University for the collaboration.
In order to establish our own processing line, I was highly supported with expertise from the MC2 cleanroom staff. I would like to thank in particular Johan Andersson, Mats Hagberg, Karin Hedsten, Göran Alestig and Ulf Södervall for their valuable support.
I thank my colleague Dr. Erik Haglund for sharing his snus with me but more importantly his profound knowledge about nanofabrication. Attila Fülöp deserves acknowledgment for fruitful discussions about integrated optics and letting me utilize his mature computer skills now and then.
I have to thank my three office mates gratefully. Dr. Josué Parra Cetina for being a great fellow, Dr. Samuel Olsson for his organized manner of answering any question and Dr. Vicente Durán Bosch for his Spanish education and positive approach towards Mondays. Special thanks are also directed to Dr. Aleš Kumpera, Dr. Tobias Eriksson and Tamás Lengyel for being around and making work more harmonic and joyful.

Furthermore, I extend thanks to Jeanette Träff for being supportive and I acknowledge of course all the rest of the photonics laboratory members for being great colleagues.
Finally, I want to express gratitude to all my family and friends.

Clemens Krückel

Göteborg
May 2017

This work was financially supported by the European Research Council Advanced Grant PSOPA (291618) and the Swedish Research Council (VR).

Abbreviations

ChGs chalcogenide glasses

CMOS complementary metal-oxide-semiconductor

CVD chemical vapor deposition

CW continuous wave

DFB distributed feedback

DUV deep ultraviolet

ebeam electron-beam

EUV extreme ultraviolet

FCA free-carrier absorption

FWM four-wave mixing

GVD group-velocity dispersion

HNLF highly nonlinear fiber

IC integrated circuit

IR infrared

LPCVD low-pressure chemical vapor deposition

MBE molecular beam epitaxy

MEMS micro-electro-mechanical systems

MOCVD metalorganic chemical vapor deposition

MOSFET metal-oxide-semiconductor field-effect transistor

NA numerical aperture

PECVD plasma-enhanced chemical vapor deposition

RF radio-frequency

RIE reactive-ion etching

SBS stimulated Brillouin scattering

SEM scanning electron microscopy

SHG second-harmonic generation

SOA semiconductor optical amplifier

SOI silicon-on-insulator

SPM self-phase modulation

SSMF standard single-mode fiber

THG third-harmonic generation

TPA two-photon absorption

UV ultraviolet

VCSEL vertical-cavity surface-emitting laser

XPM cross-phase modulation

Contents

Chapter 1

Introduction

Our society displays a huge demand for high-speed internet. This demand is satisfied, in part by the technological achievements made in the field of optical communication. This field involves the transmission of digital information via light over fibers of glass. Thereby, light is routed through a global network of optical fibers in order to connect computers and data centers all over the world. The advent of fiber technology in 1966 [1] enabled a revolution in modern communication leading to the present fiber links with outstanding data rates beyond 1 Tb/s.
The optical fiber is the standard medium used to transmit data in long distance connections of metro and long-haul links between cities and continents. Furthermore, the fiber is also essential in connections of shorter range, like in data centers or supercomputers. Indeed, the fiber has progressively replaced most metal-based transmission lines (e.g. copper) for distances down to 1 m [2]. Interestingly, it was already predicted in 1984 [3] that the optical connection is the best solution to connect silicon electronic components. The reason for this is that an optical connection has about six orders of magnitude lower loss at high data rates compared to an electrical connection [4].
Data centers are huge facilities for data storage and data processing driven by social media platforms or search engines. The large number of servers in a data center are commonly linked by fiber-based optical interconnects [2]. Currently there are two methods to realize an optical interconnect, based on either vertical-cavity surface-emitting lasers (VCSELs) or silicon photonics. The VCSEL, based on III-V materials, is a laser source that offers high-speed direct on-off switching to modulate binary optical data [5, 6]. Companies like TE connectivity utilize the VCSEL technology in their optical interconnects to reach data rates of 4×25 Gb/s [7]. The silicon photonics approach on the

other hand utilizes an laser in combination with a silicon based modulator integrated on a microchip. There are many companies developing silicon photonic interconnects for datacenters. For example, Sicoya has presented their 4×25 Gb/s transceiver based on silicon photonics technology [8]. The major requirements for the platforms used in data centers are low-cost fabrication, low-power consumption, high reliability and simple scalability to higher data rates. In [9] both platforms, VCSEL and silicon photonics, are compared from a technological and economic perspective. The prediction foresees that silicon photonics is favored for longer transmission distances (>300 m) with single-mode fibers and VCSELs continue its domination for data centers due to economical benefits.

In the context of this thesis, it is meaningful to present the field of silicon photonics in more detail. Silicon photonics is the integration of optical devices on a silicon microchip. For the integration of optical devices the same nanofabrication facilities are utilized as for the high-volume integration of silicon microelectronics. Silicon microelectronics, more precisely the complementary metal-oxide-semiconductor (CMOS) transistor logic, is a central key figure leading to the information revolution in the last 50 years. Especially noticeable is the massive size reduction and performance increase of electronic devices. With the demonstration of the first optical waveguide in silicon in 1986 [10], it was proven that the fabrication environment for silicon electronics can also be utilized to manufacture optical devices. In 1996 a rib waveguide was presented using the silicon-on-insulator (SOI) platform with low losses of 0.1 dB/cm showing the potential of light guiding on chip [11]. This shows that within silicon photonics even optical interconnects between processor cores at the microchip level are possible [2]. Unfortunately, silicon has no efficient light emission so by now hybrid solutions are available where III-V lasers are bonded on the silicon photonics chip [12]. An alternative solution was recently proposed in [13] where a III-V distributed feedback (DFB) laser structure was grown directly on silicon.

Nevertheless, thanks to the compatibility with CMOS fabrication facilities, tailored for high-volume low-cost processing, the fabrication of silicon photonic circuits in the same process line offers many advantages. Additionally it offers the opportunity to bring together optics and electronics on the same microchip [8]. One interesting change in recent years is the offered access to silicon photonic systems for researchers without fabrication facilities in the context of multi-project wafer runs [14]. Here production costs are shared by combining designs on the same wafer that is manufactured for all users. With multi-project wafer runs, the fabless access to silicon photonics components becomes more affordable [14].

Crystalline silicon has become a common material of choice for integrated optics. Over the past years the research output in the field of silicon photonics

for linear optical applications has increased. However, it turns out that silicon is also a very promising material for nonlinear optics applications [15]. A high refractive index and huge nonlinearities are the major advantages of this material for nonlinear integrated optics. The small core dimensions achievable with modern fabrication techniques together with the index contrast to the cladding material leads to remarkably high optical confinement, with huge intensities that enable efficient nonlinear processes. Although the market for volume production of nonlinear devices is missing, CMOS-compatible fabrication provides high yield, reproducibility and the flexibility to fabricate in existing CMOS fabs. The nonlinear optical effects can be utilized for applications like signal regeneration [16], broadband wavelength conversion [17] or supercontinuum generation [18]. However, nonlinear loss contributions that occur for wavelengths in the telecommunication band limit the performance of this material platform [19, 20].
A material platform that overcomes these challenges and does not show nonlinear losses at telecommunication wavelengths because of its large optical bandgap is silicon nitride [21]. Silicon nitride is also a CMOS-compatible material [22] and offers the same potential for mass production. Similar to silicon, silicon nitride is accessible for the broader research community through multi-project wafer runs. In its stoichiometric composition, Si_3N_4, waveguides with extraordinary low-loss performance down to 0.001 dB/cm have been demonstrated [23]. Another essential difference to silicon is the transparency window of silicon nitride. In contrast to silicon, silicon nitride is transparent down to ultraviolet (UV) wavelengths thus enabling devices for visible light processing [24] and sensing [25] applications. Silicon nitride also has a fairly high nonlinear Kerr coefficient [26]. In the past years this materials has been explored for nonlinear optics with impressive results including octave spanning comb generation [27] and ultra-broad supercontinuum generation [28]. However, fabrication challenges to achieve thick waveguides constrains the important capabilities for dispersion engineering as thick films show cracks due to high tensile stress [29]. As silicon nitride is a compound dielectric, unlike silicon, its stoichiometry can be modified during the deposition process. The change in deposition parameters allows to move from stoichiometric silicon nitride Si_3N_4 to its non-stoichiometric form by increasing the silicon content. This comes along with various advantages for nonlinear photonics.

1.1 This thesis

In this thesis we present two silicon nitride based waveguide designs. One shows thin waveguides with low-confinement and the other one thick waveguides with high confinement. For the first design we use the low-loss character-

istic to reach good nonlinear performance that leads to the first demonstration of wavelength conversion of high speed data in this platform.
With the second design of high-confinement waveguides we explore the impact of the core material on the waveguide properties. As a waveguide core material we use different LPCVD based silicon nitride compositions reaching from stoichiometric to silicon enriched. We show the first holistic study that connects fabrication and film characterization with an analysis of linear and nonlinear performance on system level. With the good nonlinear properties of the silicon rich nitride waveguide, we demonstrate supercontinuum generation and XPM-based all-optical processing.
In a theoretical analysis we compare thick waveguides based of stoichiometric silicon nitride with silicon waveguides. In the study we emphasize the impact of nonlinear absorption and set benchmarks to reach a performance target of 10 dB parametric net-gain on-chip that has not been achieved yet.

Thesis outline
In chapter 2 the basics of nonlinear optics are summarized with a focus on $\chi^{(3)}$-based Kerr nonlinearities like four-wave mixing (FWM). Chapter 3 covers the basics about waveguide theory including information about mode properties, loss and coupling mechanisms of waveguides. In chapter 4 common material platforms for integrated nonlinear optics are introduced. The platforms are compared in terms of linear and nonlinear performance and benchmarked with the highly-nonlinear fiber (HNLF) technology. Chapter 5 includes the presentation of CMOS-compatible fabrication techniques that are used to manufacture optical waveguides. In Chapter 6 possible future projects are discussed.

Chapter 2

Nonlinear Kerr optics

For high optical intensities the interaction of light and matter becomes nonlinear, meaning that the optical radiation after propagation through a medium is not a linear superposition of the radiation before the medium. Especially when working with integrated optics, a very high confinement of light can be achieved, leading to very high intensities. The resulting nonlinear effects can be utilized for useful applications. In this chapter the fundamental physical principles for nonlinear interaction of light and matter are explained with a focus on nonlinear Kerr optics, the dominant nonlinear effect in materials used for integrated optics.

2.1 Material polarization and refraction

The propagation of electromagnetic radiation is described by Maxwell's equations. In a transparent medium with no free charges Maxwell's equations become

$$\nabla \times \mathbf{E} = -\frac{\partial \mathbf{B}}{\partial t} \tag{2.1}$$

$$\nabla \times \mathbf{H} = \frac{\partial \mathbf{D}}{\partial t} \tag{2.2}$$

$$\nabla \cdot \mathbf{D} = 0 \tag{2.3}$$

$$\nabla \cdot \mathbf{B} = 0, \tag{2.4}$$

where **E** and **H** are the electric and magnetic field vectors, and **D** and **B** are the electric and magnetic flux densities [30]. The interaction of light with the medium is described by the electric displacement of charges **D** given by

$$\mathbf{D} = \epsilon_0 \mathbf{E} + \mathbf{P}, \tag{2.5}$$

where ϵ_0 is the vacuum permittivity and **P** is the induced polarization by the medium. The polarization of the material describes the reorientation and relocation of charges and dipoles in response to the presence of an electric field. As the light has a vectorial nature, the susceptibility terms are tensors and the material response depends on its orientation and isotropy. To provide a simple physical insight, a scalar mathematical description is chosen from here on.

2.1.1 Linear material properties

For a low electric-field strength in an isotropic medium, the polarization follows a linear dependence

$$P_{\text{lin}} = \epsilon_0 \chi E, \tag{2.6}$$

where ϵ_0 is the vacuum permittivity and the susceptibility χ is the proportionality factor. The susceptibility χ is related to the relative electrical permittivity of the medium ϵ_r by $\chi = \epsilon_\text{r} - 1$ which accounts for the various fundamental polarization mechanisms of the material. The excitation of the individual polarization mechanisms depends on the frequency of the present electric field therefore ϵ_r is given by a dielectric function. This frequency dependent function fully describes the optical properties of the material. The relative permittivity is a complex value

$$\epsilon_\text{r} = \epsilon_\text{r}' - i\epsilon_\text{r}'', \tag{2.7}$$

where the real part defines the strength of the polarization and the imaginary part accounts for material absorption mechanisms that occur during the polarization process. Both parts are physically linked via the Kramers-Kronig relation. Figure 2.1 illustrates the contributions to the complex permittivity (dipolar, ionic and electronic polarization mechanism) [31]. At various frequencies the polarization of the material becomes significant and the figure shows the relation between the real and imaginary part in a simplified manner. Here, we focus on the material response at high-frequency electromagnetic radiation that is relevant for materials used in the field of optics. The transparency window of these materials is given by the wavelength range in which the material absorption is negligible which is mainly restricted to the frequency spectrum between UV-radiation and IR-radiation. One way to characterize the complex dielectric function and describe the optical properties of a material is by using

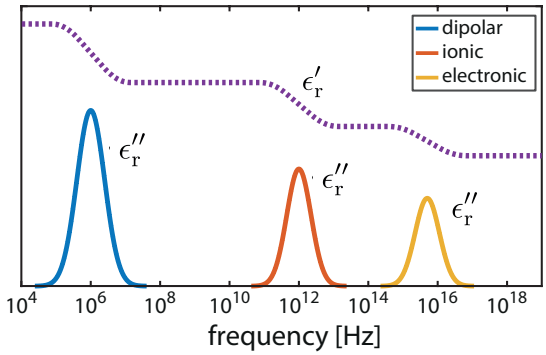

Figure 2.1: Illustration of the electrical permittivity (ϵ_r' real part, ϵ_r'' imaginary part).

ellipsometry as described in chapter 5.2. For many common optical materials like crystalline silicon or stoichiometric silicon nitride the optical constant has been studied in detail. The refractive index n_0 of the material is connected to the relative permittivity together with the relative permeability μ_r according to

$$n_0 = \sqrt{\epsilon_r \mu_r}. \tag{2.8}$$

In nonmagnetic materials $\mu_r = 1$ thus $n_0 = \sqrt{\epsilon_r}$. Similar to the relative permittivity, the refractive index is a complex parameter where the imaginary part accounts for material absorption. In Paper F we utilize the ellipsometer technology to explore the complex refractive index for various silicon nitride compositions in the UV wavelength range (more details in 5.2). This study not only gives information about one end of the transparency window, but it also defines its optical bandgap that causes linear material absorption for UV and visible light and nonlinear absorption at longer wavelengths.

2.1.2 Nonlinear material properties

For intense electrical fields a saturation of the polarization takes place and the polarization response of the material becomes nonlinear. The nonlinear polarization behavior at high intensities has its origin in the nonlinearity of the motion of molecular bound electrons in the material. The description of the polarization including nonlinear behavior is described by a pertubative approach [30]

$$P = P_{\text{lin}} + P_{\text{nl}} = \epsilon_0 \chi E + \epsilon_0 \chi^{(2)} E^2 + \epsilon_0 \chi^{(3)} E^3 + \dots \quad . \tag{2.9}$$

Here $\chi^{(2)}$ and $\chi^{(3)}$ are the second and third-order susceptibility leading to the second and third-order nonlinear polarization terms. As the higher-order susceptibility terms are in general several orders of magnitude smaller than the linear susceptibility, they only become effective at high intensities. Different susceptibility terms contribute to particular optical effects and have influence on the interaction of radiation with matter. For example, the linear susceptibility χ is included in the refractive index n_0 of the material and accounts for the change of optical phase. The second-order susceptibility $\chi^{(2)}$ leads to effects like second-harmonic generation, sum-frequency generation or the linear electro-optic effect (Pockels' effect). The third-order susceptibility $\chi^{(3)}$ results in third-harmonic generation or the quadratic electro-optic effect (Kerr effect) [31].
The Kerr effect is of great interest in this thesis. It is common to describe the strength of this effect with the nonlinear Kerr coefficient n_2 that is related to the real part of the third-order susceptibility by $n_2 = \frac{2\pi}{n_0} Re(\chi^{(3)})$ [32]. The imaginary part of the Kerr coefficient accounts for nonlinear losses in the presence of high intensity fields (i.e. TPA) originating from the optical bandgap. In [32] Sheik-Bahae et al. relate n_2 to the optical bandgap via

$$n_2 = K' \frac{G_2(\hbar\omega/E_\mathrm{g})}{n_0^2 E_\mathrm{g}^4}, \tag{2.10}$$

where K' is a constant, n_0 is the refractive index, $\hbar\omega$ is the photon energy, E_g is the bandgap energy and G_2 is a smooth function accounting for wavelength dependency with values between -0.05 and 0.1. This equation allows to predict the nonlinear Kerr coefficient from ellipsometer measurement data. In Paper F we studied this relation for different silicon nitride compositions as each composition displays a different optical bandgap E_g and a different refractive index.
The Kerr effect causes nonlinear refraction, where the refractive index of a material changes in the presence of light with high intensities. This intensity dependence of the refractive index can be described as [30]

$$n(|E|^2) = n_0 + n_2 |E|^2 . \tag{2.11}$$

As the phase shift of a wave is dependent on the refractive index given by equation 2.11, both the linear and the nonlinear part contribute to the total phase shift of a wave in a medium. In terms of nonlinear phase shift one distinguishes between self-phase modulation (SPM) and cross-phase modulation (XPM). SPM is when the nonlinear phase shift of a wave is induced by its own intensity. XPM is the nonlinear phase shift induced by the intensity of light at other frequencies or polarization. Thus the intensity modulation at a strong intensity wave leads to the phase modulation of light at a different frequency.

This can lead to practical nonlinear signal processing schemes, as studied in Paper D and E.
The nonlinear polarization of a material can give rise to generation of light at frequencies different from the one of the excitation field. Nonlinear polarization takes place in various materials of liquid, gaseous or solid state where solids may have amorphous or crystalline composition. It is important to mention that materials with molecular inversion symmetry do not posses even order susceptibility terms. This means that in materials like silicon or silicon dioxide the lowest nonlinear susceptibility term is $\chi^{(3)}$. In this thesis we refer to these materials as $\chi^{(3)}$-materials. The polarization response of the medium excited with a monochromatic electric field is illustrated in Fig. 2.2. Here an excitation field of $E(t) = E_0\cos(\omega_1 t)$ was used for convenience. For low intensity fields the polarization P follows the present field linearly without showing nonlinear behavior as shown in Fig. 2.2.a. The frequency of the output field only contains the component at ω_1 in relation to the excitation field. Increased intensities trigger the nonlinear response of the material polarization accounting for higher-order polarization terms. For a $\chi^{(2)}$-material the second-order polarization produces nonlinear distortion of the polarization. As shown in Fig. 2.2.b, the induced polarization does not follow the excitation field. This results in a new frequency component at $2\omega_1$ resulting from the squared field component in Eq. 2.9. The process in $\chi^{(3)}$-materials is similar, where a third-harmonic component is produced at $3\omega_1$ driven by the third-order susceptibility illustrated in Fig. 2.2.c [33].

2.2 Four-wave mixing

In $\chi^{(3)}$-materials the polarization is given by

$$P = \epsilon_0 \chi E + \epsilon_0 \chi^{(3)} E^3, \tag{2.12}$$

where the third-order polarization term is included. This term involves the nonlinear interaction of four waves and leads to the phenomenon of four-wave mixing (FWM). This phenomenon results from the radiation-induced modulation of the refractive index as shown in Eq. 2.11 and causes the generation of light at new frequencies. In this context, the material is mediating the nonlinear interaction among optical waves with the conservation of photon energy. In order to exemplify the four-wave-mixing process and the generation of new frequency components, we consider the input to a $\chi^{(3)}$-material as a superposition of three monochromatic waves at different frequencies as shown in Fig. 2.3.a. The mixing term of the input waves is given by $E(t) = E_1\cos(\omega_1 t) + E_2\cos(\omega_2 t) + E_3\cos(\omega_3 t)$ that is inserted into Eq. 2.12.

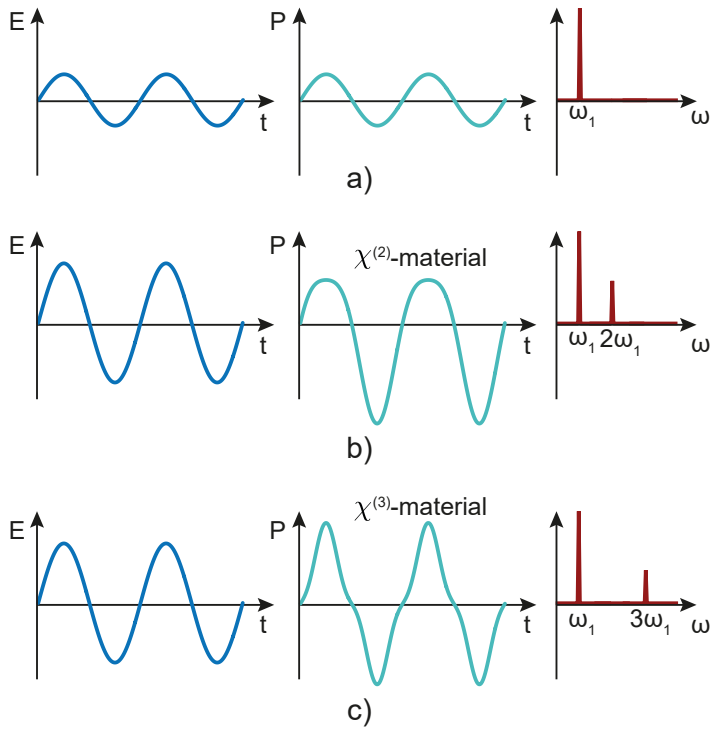

Figure 2.2: Illustration of material polarization P and frequency generation in dependence of the input field amplitude E and material susceptibility χ. a) Linear polarization of material. b) Nonlinear material polarization based on $\chi^{(2)}$ susceptibility. Second-harmonic frequency generation at $2\omega_1$. c) Nonlinear material polarization based on $\chi^{(3)}$ susceptibility. Third-harmonic frequency generation at $3\omega_1$.

The triple product of E results in multiple new frequency components at the output. All possible new frequencies (only first order) at the output of the medium are combinations of the input frequencies given by

$$
\begin{gathered}
(\omega_1+\omega_2-\omega_3),(\omega_1+\omega_3-\omega_2),(\omega_2+\omega_3-\omega_1),\\
(2\omega_1\pm\omega_2),(2\omega_1\pm\omega_3),\\
(2\omega_2\pm\omega_1),(2\omega_2\pm\omega_3),\\
(2\omega_3\pm\omega_1),(2\omega_3\pm\omega_1),\\
3\omega_1,3\omega_2,3\omega_3,(\omega_1+\omega_2+\omega_3).
\end{gathered}
$$

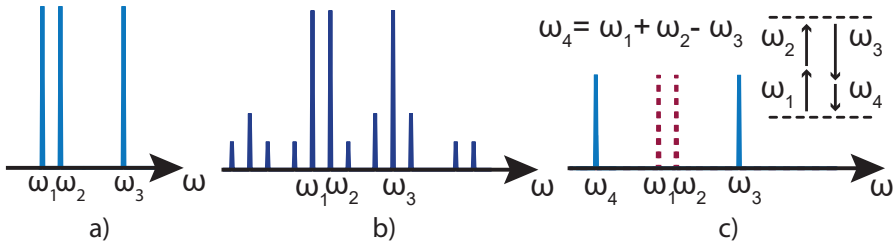

Figure 2.3: a) Illustration of spectrum with three waves at frequencies ω_1, ω_2 and ω_3. b) Illustration of frequency generation in the four-wave mixing process. c) Illustration of energy-conservation in the four-wave mixing process.

The frequency components that are generated in the FWM process are illustrated in Fig. 2.3.b (components around the third-order harmonics are not included in the figure). The efficiency of each of the above wave interactions depends on the phase-matching conditions which will be explained in section 2.4. During the FWM process the photon energy of the four-waves interacting is conserved. To illustrate this, we focus on the generated frequency component at $\omega_4 = \omega_1 + \omega_2 - \omega_3$ as shown Fig. 2.3.c. Given the photon energy of $E_{\text{photon}} = \hbar\omega$, with $\hbar$ as the reduced Planck constant, the energy is conserved if energy is transferred from two photons at frequencies ω_1 and ω_2 to photons at the frequencies ω_3 and ω_4 satisfying $\omega_1 + \omega_2 = \omega_3 + \omega_4$.

2.3 Wavelength conversion

Let us consider a common case in nonlinear optics in which the input to a $\chi^{(3)}$-material consists of a strong wave at ω_{P}, called the pump, and a weak one at ω_{S} called the signal. As the waves propagate through the medium, the signal wave may be amplified and a wave at ω_{I}, called the idler, is generated, as illustrated in Fig. 2.4. This scenario is referred to as pump-degenerate FWM. The FWM process here is similar to the example given before where the generated new frequency at ω_4 satisfies the relation $\omega_4 = \omega_1 + \omega_2 - \omega_3$. In the pump-degenerate process both photons ω_1 and ω_2 are at the same wavelength, $\omega_1 = \omega_2 = \omega_{\text{P}}$, and the signal wave is at $\omega_3 = \omega_{\text{S}}$. This means that the energy conservation in the pump-degenerate FWM process is given by [30]

$$\omega_{\text{I}} = 2\omega_{\text{P}} - \omega_{\text{S}} \tag{2.13}$$

considering $\omega_4 = \omega_{\text{I}}$. The interaction between the pump, signal and idler waves

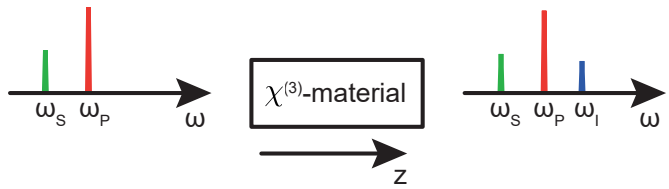

Figure 2.4: Illustration of the pump-degenerate FWM process. The propagation direction of the waves is indicated by z.

as propagating along the z-direction is described via three coupled differential equations given by [30]

$$\frac{dE_{\mathrm{P}}}{dz} = i\gamma\left\{\left[|E_{\mathrm{P}}|^2 + 2\Big(|E_{\mathrm{S}}|^2 + |E_{\mathrm{I}}|^2\Big)\right]E_{\mathrm{P}} + 2E_{\mathrm{S}}E_{\mathrm{I}}E_{\mathrm{P}}^{*}\exp\left(i\Delta\beta z\right)\right\}, \quad (2.14)$$

$$\frac{dE_{\mathrm{S}}}{dz} = i\gamma\left\{\left[|E_{\mathrm{S}}|^2 + 2\Big(|E_{\mathrm{P}}|^2 + |E_{\mathrm{I}}|^2\Big)\right]E_{\mathrm{S}} + E_{\mathrm{I}}^{*}E_{\mathrm{P}}^{2}\exp\left(-i\Delta\beta z\right)\right\}, \quad (2.15)$$

$$\frac{dE_{\mathrm{I}}}{dz} = i\gamma\left\{\left[|E_{\mathrm{I}}|^2 + 2\Big(|E_{\mathrm{P}}|^2 + |E_{\mathrm{S}}|^2\Big)\right]E_{\mathrm{I}} + E_{\mathrm{S}}^{*}E_{\mathrm{P}}^{2}\exp\left(-i\Delta\beta z\right)\right\}. \quad (2.16)$$

The coupling between the waves is facilitated by the nonlinear parameter γ and the mismatch of the propagation constant between the waves $\Delta\beta$. It is assumed that the waves have the same optical polarization and optical field overlap. The nonlinear parameter γ includes the nonlinear effects in $\chi^{(3)}$-materials and the field confinement, which is explained in more detail in section 3.5. The mismatch of the propagation constant for pump, signal and idler wave is given by $\Delta\beta = 2\beta_{\mathrm{P}} - \beta_{\mathrm{S}} - \beta_{\mathrm{I}}$ where the propagation constants of pump, signal and idler are given by $\beta_{\mathrm{P}}, \beta_{\mathrm{S}}$ and β_{I}. The propagation constant β gives information about the velocity of a wave (more detail in section 3.3).

2.4 Phase-matching condition

For efficient energy transfer between the waves in the FWM process, the conservation of momentum is required. This means that the efficiency with which power is transferred depends on the relative phase among the interacting waves. This is described within the nonlinear phase-matching condition

$$\kappa \equiv \Delta\beta + 2\gamma P_{\mathrm{P}} = 0, \quad (2.17)$$

where the linear part $\Delta\beta$ comes from the mismatch of the propagation constant between the waves and the nonlinear part $2\gamma P_{\mathrm{P}}$ accounts for the nonlinear phase shift. This equation is valid under the assumption that no pump depletion takes place and the pump power is much larger than the signal and idler power so that the main contribution to the nonlinear phase shift comes from the pump. The factor of two accounts for the pump-degenerate FWM as both annihilated pump photons are located at the same frequency. In the coupled differential equations 2.14-2.16 the nonlinear and linear phase shifts are included in the first and second terms in the parenthesis [30]. In order to compensate for the positive nonlinear phase shift, the linear phase shift has to be negative, which requires in general anomalous dispersion of the medium (dispersion is described in more detail in section 3.3.2). To achieve phase matching, the relation between power levels, propagation constants and frequencies is essential.
The efficiency of energy transfer between pump, signal and idler, when the frequency separation between pump and signal is increased, depends on the dispersion properties of the $\chi^{(3)}$-medium. One way to assess this is by evaluating how the conversion efficiency [1] changes with the wavelength separation of signal and pump. This is exemplified in Fig. 2.5 for a waveguide system with various group-velocity dispersion (GVD) values (β_2, see section 3.3.2). For smaller GVD values the conversion efficiency is maintained for a larger signal-pump detuning. The numerical simulations leading to Fig. 2.5 and ex-

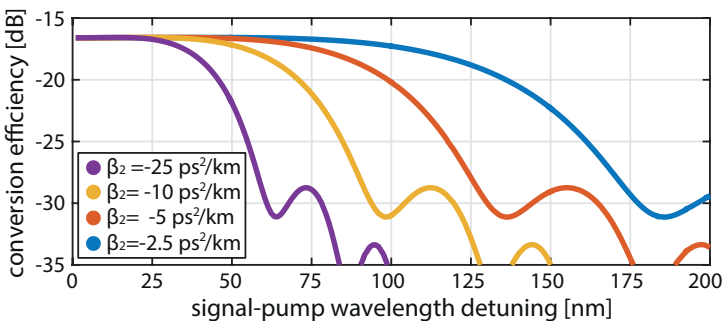

Figure 2.5: Numerical simulations of the output conversion efficiency of a 5 cm waveguide as a function of signal-pump detuning. The impact of the group-velocity dispersion (GVD) on the conversion bandwidth is shown for four different β_2 values. (Waveguide parameter: $\gamma = 5\ (\mathrm{W}\cdot\mathrm{m})^{-1}$, propagation loss = 0.5 dB/cm, Pump power = 27 dBm)

[1] Here the conversion efficiency is defined as the ratio of idler power and signal power after propagation through the $\chi^{(3)}$-medium.

periments similar to the simulations were performed in Paper A and B.
This behavior can be summarized with the conversion bandwidth Ω_{FWM}. The conversion bandwidth is defined as the signal-pump frequency separation at which the signal gain decreases by 3 dB and is given by [17]

$$\Omega_{\mathrm{FWM}} \approx \left[\frac{4\pi}{|\beta_2|\, z}\right]^{\frac{1}{2}}, \tag{2.18}$$

where β_2 is the GVD coefficient.
With either low GVD or short interaction length z, the conversion bandwidth can be increased. One huge advantage of integrated optical systems is the potential for strong light confinement that results in the possibility to tailor the dispersion properties in a reliable manner. In combination with the short length of these systems, it is possible to achieve a very large conversion bandwidth. To give an example, by dispersion engineering the waveguide, broadband wavelength conversion over ~ 200 nm has been shown in an integrated silicon waveguide [17].

Chapter 3

Waveguide theory

Integrated optical systems offer the opportunity to tailor the dispersion and achieve high confinement in small structures, therefore leading to high optical intensities at moderate power levels. These are ideal conditions for the realization of nonlinear optics with high efficiency and over broad bandwidth. In this chapter wave guiding structures and their basic physical properties are introduced.

3.1 Confined-wave propagation

The propagation of an optical beam in free space or bulk media is accompanied by the phenomenon of diffraction. This phenomenon describes the spatial broadening of optical radiation upon propagation. Waveguiding structures provide a means to avoid the divergence associated to this effect and guide light in a confined manner over distance. Waveguides are composed of mainly two distinct regions, a core medium enclosed by a cladding. The two areas are distinguished by a refractive index difference, where the core displays a higher refractive index than the surrounding cladding. Crucial for wave guiding is the behavior of light at the interface of the two regions. The confinement upon propagation can be understood from a ray-optics picture, where the energy of the wave confined in the core experiences total internal reflection at the interface with the cladding [34]. The propagation of light in a waveguide is described by the wave equation [30]

$$\nabla^2\mathbf{E} = \frac{1}{c^2}\frac{\partial^2\mathbf{E}}{\partial t^2} - \mu_0\frac{\partial^2(\mathbf{P}_{\mathrm{lin}})}{\partial t^2} - \mu_0\frac{\partial^2(\mathbf{P}_{\mathrm{nl}})}{\partial t^2}. \tag{3.1}$$

The wave equation is derived from Maxwell's equations. The electric field and the material polarization are given by $\mathbf{E}$ and $\mathbf{P}$, the speed of light in vacuum is c and the vacuum permeability is μ_0. The Nabla-operator ∇ represents the differential operation $(\frac{\partial}{\partial x}, \frac{\partial}{\partial y}, \frac{\partial}{\partial z})$ for the spatial directions x, y and z.

3.2 Waveguide designs

The light guiding by total internal reflection requires a refractive index difference between the core and cladding materials. In order to achieve this index contrast, the proper materials have to be chosen. Several different platforms provide the required refractive index features, and various different waveguide designs have been developed that offer confined light propagation. One important design, essential for the success of optical communication, is the optical fiber where core and cladding are circular rods presented in Fig. 3.1.a. In the figure, z indicates the propagation direction of the optical wave. The material of choice for typical optical fibers is fused silica with slightly different composition of core and cladding. The refractive index difference is only around 0.01 and a common core diameter of a standard single-mode fiber (SSMF) used for telecommunications is around 10 µm.
It is important to distinguish the fiber design from designs suitable for inte-

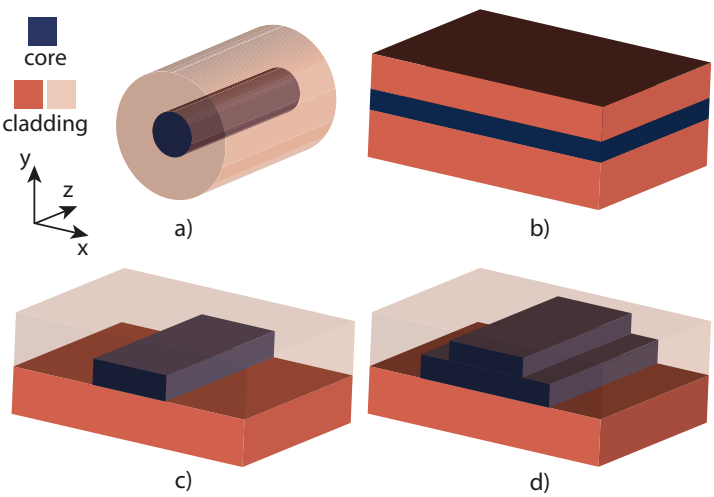

Figure 3.1: Schematics of basic waveguiding geometries. a) Optical fiber. b) Planar waveguide. c) Strip waveguide. d) Rib waveguide.

gration in micro- and nanoprocessing facilities. As fibers are drawn from a preform with proper core-cladding composition, the cylindrical design form is favorable. In contrast to this, integrated waveguide designs are based on planar layer deposition and structuring. Suitable basic designs for the integration are presented in the following. A fundamental waveguide that is the base for elementary calculations of the electromagnetic field in the structure is the planar waveguide shown Fig. 3.1.b. This is the simplest design for integrated waveguides as it consists of three unprocessed stacked layers. The index difference between core and cladding allows light confinement in the vertical direction, but confinement in the horizontal direction can not be achieved in this design. To confine the light in the transverse and lateral direction, the core medium has to be surrounded by cladding material in both x- and y-direction. The strip waveguide design illustrated in Fig. 3.1.c enables this. Width and height of the waveguide can be varied in the manufacturing process. For this design one etching step is required in order to pattern the core in the horizontal direction. With the strip waveguides it is possible to achieve waveguide bends allowing the routing of light on chip and the design of more advanced photonic systems. Another popular waveguide design for confinement in x- and y-directions is the rib waveguide shown in Fig. 3.1.d. In comparison to the strip waveguide this design requires two etching steps. A similar design is used to remove free charge carriers from the waveguide center as discussed in Paper G (see 3.4.2 for more information about free-carrier absorption (FCA)). However, the main waveguide design presented in all appended Papers A−G is the strip waveguide.

3.3 Mode properties

3.3.1 Mode field

As light propagates in a waveguide, only specific transverse field distributions of the electromagnetic field can be propagated. These field distributions are termed the modes of the waveguide. Information about the modes is obtained by solving the wave equations (Eq. 3.1) for the concrete combination of waveguide design and material distribution. Only a few structures, such as the cylindrical geometry and the slab waveguide allow for an analytical treatment. Otherwise, this equation needs to be solved numerically given the boundary conditions and specific material information. The number of modes in the waveguide varies, depending on the optical wavelength, the waveguide dimensions and the used materials. If only the fundamental mode propagates, the waveguide is called single mode. In order to simplify matters, a solution of

the wave equation is approximated with a uniform transverse-field distribution propagating in the z direction as given by

$$E(x, y, z) = E(x, y)\exp(i\beta z). \tag{3.2}$$

Here $E(x, y)$ represents the spatial field distribution transverse to the propagation direction and β indicates the propagation constant of the mode. Both parameters are characteristic for the mode and describe the propagation of the electromagnetic field completely. Only a single frequency component of the electrical field is considered, and the harmonic term $\exp(-i\omega_0 t)$ is dropped for simplicity.
How well the optical field is confined inside the core area is described by the effective area parameter [30]

$$A_{\text{eff}} = \frac{\left(\int_{-\infty}^{\infty}\int_{-\infty}^{\infty} |E(x,y)|^2 \, dxdy\right)^2}{\left(\int_{-\infty}^{\infty}\int_{-\infty}^{\infty} |E(x,y)|^4 \, dxdy\right)}. \tag{3.3}$$

As can be seen in the equation, the field distribution $E(x, y)$ is what determines the effective area. The modal field distribution is dictated by the waveguide design and the index contrast between the core and the cladding. Paper F shows how A_{eff} changes with a different refractive index of the waveguide core. In general, higher-order modes and longer wavelengths result in larger effective areas. As a comparison, a typical SSMF has an effective area of around 100 μm^2, whereas a silicon strip waveguide can reach an effective area of 0.054 μm^2 as reported in [35].

3.3.2 Dispersion

The propagation of light in bulk media is affected by the refractive index n_0 of the medium. The dependence of the refractive index on the wavelength is the chromatic dispersion of the material. In integrated waveguides the optical phase shift of light can be different from the one occurring in bulk media. This is accounted for by introducing the effective index n_{eff} as

$$n_{\text{eff}} = \frac{\beta}{k_0}, \tag{3.4}$$

where $k_0 = \frac{2\pi}{\lambda_0}$ is the wavenumber with λ_0 the wavelength of light in vacuum. Different modes and modes at different polarization have different effective indices n_{eff}. The effective index accounts for the influence of core and cladding

materials and the waveguide design. The effective index of a guided mode has a value in between the refractive index of the cladding n_{cl} and the core n_{cl}, i.e. $n_{\mathrm{cl}} < n_{\mathrm{eff}} \leq n_{\mathrm{co}}$. As n_{eff} is wavelength dependent, both the material dispersion and the waveguide contribute to the total dispersion. More detailed information about dispersion in the waveguide is revealed when writing β as a Taylor expansion around a center frequency ω_0 [30]

$$\beta(\omega) = \beta_0 + \beta_1(\omega - \omega_0) + \frac{1}{2}\beta_2(\omega - \omega_0)^2 + \dots \quad . \tag{3.5}$$

The terms β_m account for different contributions to the propagation constant and are calculated by

$$\beta_{\mathrm{m}} = \left(\frac{d^{\mathrm{m}}\beta}{d\omega^{\mathrm{m}}}\right)_{\omega=\omega_0} . \tag{3.6}$$

The parameter β_0 is connected to the phase velocity of a monochromatic wave by $v_{\mathrm{p}} = \frac{\omega_0}{\beta_0}$. The group velocity of a pulse is related to β_1 by $v_{\mathrm{g}} = 1/\beta_1$. Information about how pulse broadening is affected upon propagation is connected to the amount and sign of the group-velocity dispersion (GVD) coefficient β_2. The broadening comes from the different propagation speeds of the individual frequency components forming a pulse. One distinguishes between normal dispersion when the GVD is positive ($\beta_2 > 0$) and anomalous dispersion when the GVD is negative ($\beta_2 < 0$). Sometimes this is called normal GVD and anomalous GVD. In the anomalous dispersion regime the higher frequency (blue-shifted) components propagate faster than the lower frequency (red-shifted) components of an optical pulse. The reverse is true for the normal dispersion regime. The sign of the GVD coefficient is important for phase-matching in nonlinear optics (see 2.4). It is highly relevant to re-emphasize that for high confinement waveguides the GVD depends on the waveguide parameters, and the dispersion can be tailored e.g. by changing the dimensions of the waveguide. In Paper B and F simulations were presented, that show the dependence of the GVD on the waveguide dimensions of a strip waveguide. It is common to describe the GVD with the dispersion parameter D where

$$D = \frac{d\beta_1}{d\lambda} = -\frac{2\pi c}{\lambda^2}\beta_2 \tag{3.7}$$

and the units are typically expressed in ps/(nm·km).

3.3.3 Polarization

The electromagnetic wave description assigns a direction of oscillation to the electric and magnetic field component as it propagates in time and space. In isotropic media the propagation behavior, more precisely the propagation constant, is independent on the electromagnetic field oscillation. However,

in anisotropic media the refractive index is dependent on the orientation of the electric field, leading to birefringence. It is common to define the electric field as the superposition of two polarization states, the TE and the TM polarization modes. For the TE polarization the electrical field component in propagation direction is zero and for TM polarization the magnetic field component in propagation direction is zero [36].
Although the materials forming a waveguide are mostly isotropic, the waveguide itself can however show anisotropic optical properties. This can be the case in rectangular waveguides. As the field components along the propagation direction are only close to zero, one talks about quasi-TE and quasi-TM modes. In addition, for structures with a small refractive index difference between core and cladding, the two polarization states (quasi-TE and quasi-TM) have dominant electric field components either in the horizontal x-direction or vertical y-direction labeled by E^x_{pq} and E^y_{pq}, where p relates to the mode-order in x-direction and q relates to the mode-order in y-direction. In order to exemplify the difference of the effective index on the mode order and polarization, the modes that are present in an integrated strip waveguide with dimensions of 1 000 nm in width and 500 nm in height are compared in Fig. 3.2. A mode-solver was used to calculate the modes. The simulations were carried out using COMSOL Multiphysics where Maxwell's equations are solved using a finite element method. The waveguide, here silicon nitride as the core material and silicon dioxide as the cladding material, has two guided modes for both states of polarization at 1.55 µm wavelength. The figure shows the power distribution in the propagation direction and it can be seen that the effective index changes with the state of polarization and mode order. In applications, the birefringent dependence of the waveguide design has been utilized to build integrated photonic systems like polarization rotators and polarization splitters [37, 38], as well as polarizers [39]. Even polarization independent designs have been demonstrated [40].

3.4 Loss mechanisms

3.4.1 Linear loss

The propagation loss in integrated optical waveguides has three fundamental linear contributions which are material absorption, scattering loss and radiation loss [41]. The origin of material losses and the resulting transparency window of optical materials has been introduced in section 2.1.1 and studied for silicon nitride in Paper F. The loss contributions are accounted for in the

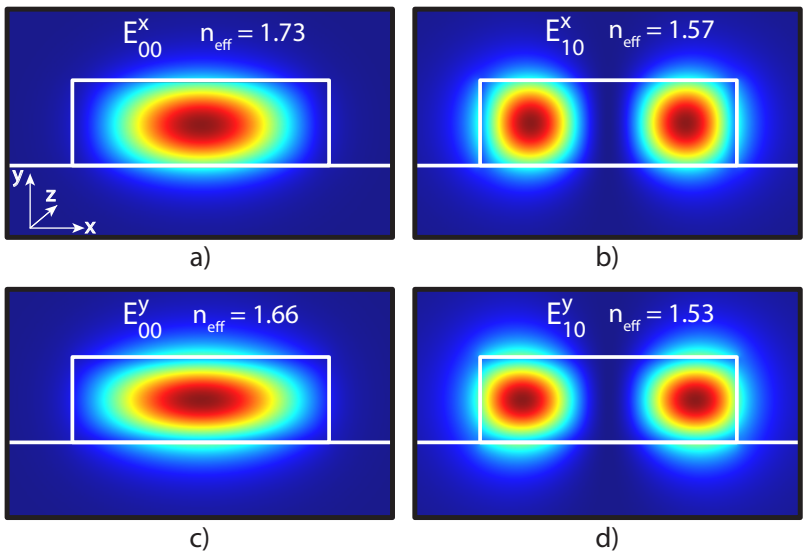

Figure 3.2: Mode-solver simulations of the power distribution in propagation direction z for a strip waveguide with dimensions of 1000 nm in width and 500 nm in height. The core and cladding materials are silicon nitride and silicon dioxide. a) Fundamental quasi TE-mode (E^x_{00}). b) Second-order quasi TE-mode (E^x_{10}). c) Fundamental quasi TM-mode (E^y_{00}). d) Second-order quasi TM-mode (E^y_{10}).

loss parameter α that leads to an exponential power decay along propagation distance z

$$P = P_0 \exp(-\alpha_{\text{lin}} z), \tag{3.8}$$

where P_0 is the initial power before propagation and α_{lin} is the linear attenuation coefficient[1]. In nonlinear optics, the propagation loss plays a significant role. In calculations of nonlinear processes the total physical length of the waveguide L is commonly replaced by the effective length L_{eff} given by

$$L_{\text{eff}} \equiv \frac{1 - \exp(-\alpha_{\text{lin}} L)}{\alpha_{\text{lin}}}. \tag{3.9}$$

The effective length represents the waveguide length before the power attenuation becomes significant. With a longer physical length L the effective length increases according to Eq. 3.9 and reaching a maximum that is given by $1/\alpha_{\text{lin}}$.

[1]The conversion from attenuation in dB/m to linear attenuation is given by the relation $\alpha \approx 4.343 \cdot \alpha_{\text{lin}}$.

In Fig. 3.3.a this is illustrated for different loss values.

The origin of material absorption lies in the interaction of optical waves with the medium during propagation as introduced in 2.1.1. Impurities in the material can lead to additional absorption. A known example for a molecular-bond-related absorption wavelength is the nitrogen-hydrogen bond (N-H) whose oscillation behavior absorbs light around telecom wavelengths. In Paper F we show that a high-temperature annealing step can remove this absorption mechanism as has been demonstrated before.

Another contribution to the propagation loss is the scattering loss that occurs at the interfaces between the core and the cladding. The amount of scattering loss is related to the mean value of the surface roughness and its statistical variance [42]. The confinement of light, and thus the interaction with the sidewall, changes with core-cladding index contrast, mode order, wavelength and polarization. Waveguides with very thin sidewalls of only $40 - 50$ nm lead to record low propagation loss [23]. A similar core thickness has been used in the work of Paper A. In Paper B the roughness of the waveguide sidewalls and top surface has been analyzed in order to characterize the scattering loss. Another origin of scattering loss are imperfections in the core material.

The third contribution to propagation loss, the radiation loss, becomes relevant when waveguides are bent. In a curved waveguide the optical field is distorted in comparison to a straight waveguide which can lead to radiation of optical energy into radiating modes. The radiation loss becomes larger for shorter bending radii and waveguides with lower light confinement [43]. Therefore, in

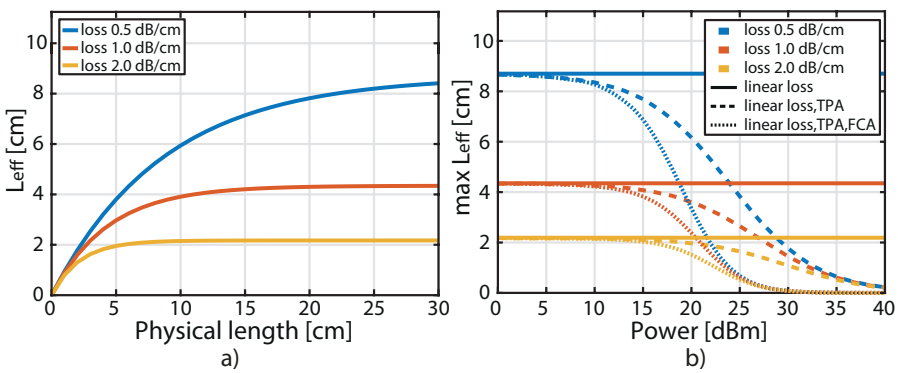

Figure 3.3: a) Impact of linear propagation loss on the effective length (L_{eff}). b) Impact of linear propagation loss, two-photon absorption (TPA) and free-carrier absorption (FCA) on the maximum effective length as a function of optical power (More details in text).

integrated optical systems, the minimum achievable bending radius is mainly limited by radiation loss rather than by processing tolerances [41]. For high-density integrated photonics a high optical confinement is essential in order to implement waveguides with short bending radii ($\leq$10 µm).

3.4.2 Nonlinear loss

Nonlinear loss contributions become relevant in certain materials. In the presence of nonlinear loss, the total loss coefficient changes to

$$\widetilde{\alpha} = \alpha + \alpha_{\mathrm{NL}}(|E|^2), \tag{3.10}$$

where α describes the linear contribution to the loss and α_{NL} accounts for nonlinear loss. Examples of nonlinear loss is interband absorption like two-photon absorption (TPA) that occurs in materials like silicon or chalcogenide glasses (ChGs) at telecommunication wavelengths owing its small optical bandgap [19, 44]. During the TPA process the energy of two photons is absorbed in order to bridge the bandgap energy and excite electrons from the valence band to the conduction band. This nonlinear loss has intensity dependence according to

$$\alpha_{\mathrm{NL(TPA)}} = \alpha_2 \left|E\right|^2, \tag{3.11}$$

where α_2 is the TPA absorption coefficient. The free charge carriers generated by TPA give rise to another nonlinear loss mechanism, the free-carrier absorption (FCA). In this process photon energy is transferred to free carriers in the conduction band or holes in the valence band. The impact of TPA and FCA on the maximum effective length is illustrated for a silicon waveguide[2] in Fig. 3.3.b. In the scenario of nonlinear loss the maximum effective length is defined as the length at which the power decayed by 4.343 dB. The figure shows the dependence on the optical power and a comparison to materials without nonlinear loss. The optical confinement defines the intensity for a given power according to $|E|^2 = P/A_{\mathrm{eff}}$. The emerging free-carrier loss is proportional to the free-carrier concentration [41] and reduced with the duration it takes for carrier recombination (free-carrier lifetime). A possible way to counteract the FCA and effectively reduce the free-carrier lifetime is the removal of free carriers from the waveguide region. This has been shown in devices based on a reverse biased p-i-n structure in rib waveguides [45]. How the nonlinear absorption in silicon waveguides (with or without carrier removal) changes the achievable nonlinear phase shift (see 3.5) has been studied theoretically in Paper G.

[2]The following parameters were used for simulations: $\gamma = 200$ $(\mathrm{W{\cdot}m})^{-1}$, $A_{\mathrm{eff}} = 0.09$ µm^2, $\alpha_2 = 7\,000{\cdot}10^{-15}$ m/W, free-carrier lifetime = 800 fs.

3.4.3 Coupling loss

The coupling of light from an optical fiber to an integrated waveguide is commonly done by the direct focusing (end-fire) approach or by grating couplers. In the end-fire coupling approach light is focused directly from the fiber to the bare integrated waveguide. The coupling efficiency is dependent on the overlap integral of the field of the incident beam and the mode field of the waveguide and is calculated by [41]

$$\eta_{\mathrm{m}} = \frac{\left(\int A(x) B_{\mathrm{m}}^{*}(x) dx\right)^{2}}{\int A(x) A^{*}(x) dx \int B_{\mathrm{m}}(x) B_{\mathrm{m}}^{*}(x) dx}. \tag{3.12}$$

To simplify the equation only the transverse direction is considered, where $A(x)$ and $B_{\mathrm{m}}(x)$ are the field distributions of the incident beam and the m-th mode of the waveguide. The equation shows that improved coupling is achieved by matching the two fields $A(x)$ and $B_{\mathrm{m}}(x)$.
Spot size converters at the end of the waveguides are commonly used to tailor the mode field in the integrated system to match the one of the incident beam. In [46] a coupling loss of 0.2 dB per facet has been demonstrated using a spot size converter. In this thesis, we used direct side-coupling into the waveguides via tapered lensed fibers.
Grating couplers are periodic grating structures that allow coupling of light from an oblique angle to the direction of the waveguide [47]. The advantage of grating couplers in comparison to end-fire coupling is that cleaving of the wafer is not needed, thus making on wafer testing possible. A drawback is the limited bandwidth and polarization dependence. In [48] a grating coupler design with a coupling loss of 0.62 dB and a 1-dB bandwidth of 40 nm has been shown.

3.5 Nonlinear parameter

It is convenient to write the nonlinear behavior of an integrated waveguide in the nonlinear parameter γ as

$$\gamma = \frac{2\pi n_2}{\lambda A_{\mathrm{eff}}}, \tag{3.13}$$

where n_2 is the Kerr coefficient of the material, λ is the wavelength and A_{eff} is the effective area. The equation shows that both the nonlinear Kerr properties of the material and the field confinement have significant contributions to γ. With a given nonlinear parameter γ, power P and effective length L_{eff}, the maximum nonlinear phase shift in a waveguide is

$$\theta_{\mathrm{nl}} = \gamma P L_{\mathrm{eff}}. \tag{3.14}$$

This was presented in Paper F where both the increase in nonlinear Kerr coefficient and the reduction of effective area leads to a larger nonlinear parameter.

Chapter 4

Materials for integrated nonlinear optics

In this chapter we present and compare material platforms that are established in the field of integrated nonlinear optics. The materials are classified into three different groups: Chalcogenides, III-V materials and CMOS-compatible materials. In the following, linear and nonlinear optical properties are presented and afterwards the materials are compared to one of the most common widespread solutions for nonlinear optics, i.e. a highly nonlinear fiber (HNLF) of silicon-doped glass that is commercially available.

4.1 Chalcogenides

The family of chalcogenide glasses (ChGs) is based on the chalcogen elements from group VIa of the periodic table presented in Fig.4.1 [44]. In particular the elements sulphur, selenium and tellurium form glass compounds with elements like phosphorous, germanium or arsenic. To form the glass compounds, deposition techniques like thermal evaporation, sputtering or chemical vapor deposition (CVD) can be used, followed by a post-deposition annealing step. ChGs are amorphous semiconductors and by tailoring the atomic composition of the glasses the optical properties can be changed. For instance the transparency of the ChGs is affected by the used chalcogen element, and the transparency window can enter into the mid-infrared wavelength region (sulphides 11 µm, selenides 15 µm, tellurides 20 µm) [44]. With a linear refractive index of $\sim 2-3$ at 1.55 µm wavelength, these glasses can be used as the core medium in an integrated optical waveguide with different surrounding cladding materials, such as SiO_2.
Examples for ChGs are the selenium based compound GeAsSe and the sulphur-

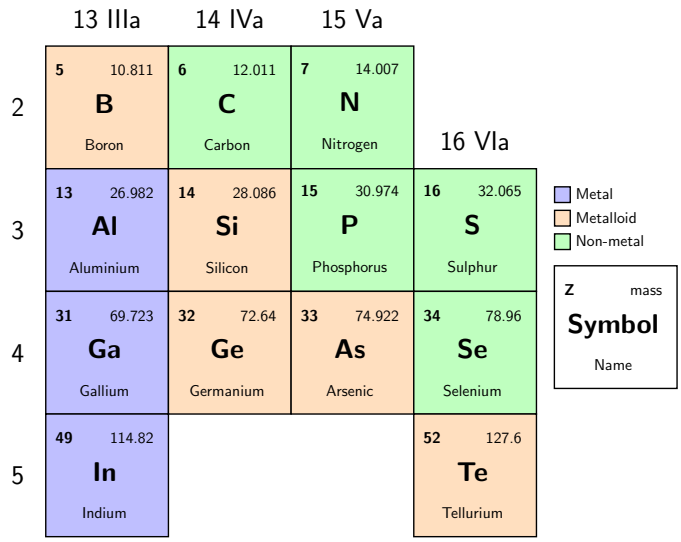

Figure 4.1: Selected section of the periodic table with relevant materials for integrated nonlinear optics.

based compound As_2S_3. The glass GeAsSe has very high Kerr nonlinearities of up to $9 \cdot 10^{-18}$ m^2/W with a very low two-photon absorption (TPA) coefficient [49, 50]. Waveguides created with this material have been used to demonstrate FWM and supercontinuum generation [49]. A more common chalcogenide material in the field of integrated nonlinear optics is As_2S_3. Although it has a three times lower Kerr coefficient than GeAsSe, the lower waveguide losses achieved while having similar low TPA make it the more suitable ChGs for applications in the telecommunication band [51]. Waveguides based on As_2S_3 have been fabricated with 5 dB/m propagation loss compared to 250 dB/m for GeAsSe (see Table 4.1). Using rib waveguides made from As_2S_3, several nonlinear applications have been shown, like FWM [52, 53] or supercontinuum generation [51], and applications like wavelength conversion based on XPM [54] and FWM [55] as well as SPM-assisted signal regeneration [56].

4.2 III-V materials

The group of III-V materials is based on compounds formed between elements from group IIIa (aluminum, gallium or indium) and group Va (nitrogen, phosphorous, arsenic) in the periodic table shown in Fig.4.1. Due to the direct bandgap in III-V materials they are commonly used in amplifiers (semiconductor optical amplifiers (SOAs)) or light emitting devices, including lasers. The

crystalline semiconductor materials are mainly grown by molecular beam epitaxy (MBE) or metalorganic chemical vapor deposition (MOCVD) in order to achieve layer by layer growth of crystalline morphology. This epitaxial growth requires a crystalline substrate and misses flexibility of stacked deposition on top of non-crystalline materials. Using III-V materials in CMOS-process lines is strictly avoided due to contamination of the fabrication line as III-V elements serve as dopants for silicon.
III-V materials like GaAs or AlGaAs are transparent through the communication bands and are utilized for nonlinear integrated optics. As the materials form compounds, the optical properties can be varied by changing the atomic composition of the compound. For instance, both the refractive index and bandgap increases by adding Aluminum to GaAs, hence becoming AlGaAs. The nonlinear coefficient of these materials is very high with $16 \cdot 10^{-18}$ m^2/W for GaAs [57] and even $26 \cdot 10^{-18}$ m^2/W for AlGaAs [58]. However, in the compound of GaAs, large nonlinear loss $\sim 100\,000 \cdot 10^{-15}$ m/W [20] limits the amount of power that can be sent to the device. A significant reduction of nonlinear loss by more than one order of magnitude is achieved with increased content of aluminum in AlGaAs [59] because of the increase in bandgap. The high nonlinearities and moderate linear propagation losses enable nonlinear experiments in AlGaAs like FWM [59, 60]. Wavelength conversion assisted by XPM has been shown in waveguides [57] as well as in resonators [61]. Even microresonator based comb generation has been shown [58]. In AlGaAs outstanding performance has been achieved by demonstrating a FWM conversion bandwidth of 750 nm [62] and a very low power threshold (7 mW) for comb generation [63].

4.3 CMOS-compatible materials

The manufacturing facilities for CMOS electronics have matured over the last decades and allow for low cost and mass production of electronic devices. Silicon, a group IV element, is the base material for CMOS components [64] but it is also attractive for nonlinear integrated optics [15] due to its large transparency window between 1 and 9 µm wavelength and its large nonlinear Kerr coefficient. A description of CMOS-compatible processing is given in more detail in the next chapter. In the field of nonlinear integrated optics, pure silicon is used both in crystalline and amorphous morphology. Silicon is also used in a compound with nitrogen (group V), forming silicon nitride, which is another CMOS-compatible material widely used for nonlinear integrated optics.

4.3.1 Silicon

Crystalline silicon

Integrated silicon waveguides are mainly based on the commercially available silicon-on-insulator (SOI) platform. This platform, originating from CMOS electronics, offers a single-crystalline silicon film separated by a layer of silicon dioxide from the bulk substrate. This layer combination is not possible to fabricate by deposition, but achieved by wafer bonding [65] and is most suitable for the fabrication of waveguides. Crystalline silicon (c-Si) offers a large Kerr coefficient of $4 - 9 \cdot 10^{-18}$ m^2/W [19, 20]. A high refractive index contrast is given when silicon (3.5 at 1.55 µm wavelength) is embedded in silicon dioxide (1.45 at 1.55 µm wavelength). Under this condition the light guided in the silicon core is highly confined which leads to high optical intensities. The drawback of silicon as a material for nonlinear optics is the low optical bandgap of 1.2 eV leading to a TPA coefficient of $\sim 5\,000 \cdot 10^{-15}$ m/W in the telecommunication band [19, 20]. Upon TPA, free carriers are generated in the waveguide which causes further absorption loss and a shift in dispersion. The resulting free-carrier absorption sets a limit on the maximum intensity level where efficient nonlinear processes are possible. The nonlinear absorption becomes less critical at longer wavelengths where the photon energy is reduced (e.g. 0.62 eV at 2 µm wavelength). For nonlinear optics in the mid infrared (IR), silicon is a very suitable material.

Free carriers can be removed from the waveguide core with an applied electric field [66, 67]. In order to apply the electric field, a reverse-biased p-i-n diode design is used in a rib waveguide structure. Nonlinear experiments that have been presented in SOI-based silicon waveguides with and without carrier removal design include, among others, signal regeneration [16, 68], supercontinuum generation [18] and third-harmonic generation (THG) [69]. Furthermore FWM has been demonstrated in nonresonant structures [70–72] as well as in microring resonators [73, 74]. Wavelength conversion with data rates up to 40 Gb/s has been shown in [75, 76]. It is worth highlighting that in crystalline silicon the highest continuous wave (CW) FWM conversion efficiency (-1 dB) has been achieved among all waveguide platforms by using a biased p-i-n diode for carrier removal [45]. In Paper G we theoretically compared silicon waveguides (with and without carrier removal) in terms of their nonlinear performance and compared it to stoichiometric silicon nitride.

Amorphous silicon

Low-temperature-deposited silicon in amorphous form has raised interest in recent years because of its increased nonlinear Kerr coefficient and reduced TPA coefficient compared to crystalline silicon. The deposition in a plasma-enhanced chemical vapor deposition (PECVD) step (further information in 5.5.2) allows processing temperatures as low as $200 - 400°C$. The possibility

of deposition, that is not given for crystalline silicon, allows the fabrication of multiple layer designs and possible vertical coupling between waveguides. Deposited amorphous silicon has dangling bonds[1] that are commonly saturated with hydrogen leading to hydrogenated amorphous silicon (a-Si:H) suitable for integrated optics [77]. One drawback of amorphous silicon is its temporal instability. Although material degradation can be reversed by annealing, a variation of system performance can be expected [78]. Indeed, reported nonlinear Kerr coefficients for a-Si:H vary in the range of $0.5 - 74.3 \cdot 10^{-18}$ m^2/W [79–84] indicating a large dependence of the material on the processing parameters. TPA coefficients of around $1\,000 - 3\,000 \cdot 10^{-15}$ m/W have been presented [79–82] that is roughly a factor of two below crystalline silicon. The potential for nonlinear optics has been shown in e.g. FWM experiments [81, 85] and FWM based wavelength conversion [80]. Additionally spectral broadening induced by SPM [83] and XPM [79] has been presented, as well as supercontinuum generation [86, 87].

4.3.2 Silicon nitride

Another CMOS-compatible material that is widely used to integrate nonlinear photonic systems is silicon nitride. In the CMOS fabrication process silicon nitride is used as a thermal and electrical insulator. Silicon nitride can be deposited in low-pressure chemical vapor deposition (LPCVD) and plasma-enhanced chemical vapor deposition (PECVD) process steps (details about both processes are provided in 5.5) as well as by sputtering. With these different techniques the material deposition can be performed at various temperatures giving large flexibility of fabrication. The material has in general amorphous morphology. The elementary material composition is crucial when characterizing its optical properties. In the field of nonlinear photonics three main groups of silicon nitride have been presented: stoichiometric silicon nitride Si_3N_4 with a given atomic Si:N ratio of 3:4 studied in Paper A, F and G; silicon nitride in a non-stoichiometric composition with varying atomic ratios summarized with Si_xN_y, studied in Papers B−F; and a proprietary material named Hydex, whose properties are similar to silicon oxynitride SiON [22]. In the following all three material platforms are presented in detail.

Stoichiometric silicon nitride

Stoichiometric silicon nitride has a transparency window ranging from below 0.3 to above 6 µm wavelength, and it has potential as a core material for integrated optics, including visible light applications. The refractive index of stoichiometric silicon nitride is ~ 2 at 1.55 µm wavelength. Waveguides

[1] Dangling bonds are unsaturated material bonds that have energy states within the bandgap of the material resulting in strong absorption in the near IR [77].

manufactured with Si_3N_4 and SiO_2 as core and cladding materials show low propagation losses and good optical confinement reaching high intensity and long interaction lengths. Among all presented materials, this platform provides waveguides with the lowest propagation loss of 0.001 dB/cm [23] and ring resonators with the highest Q-factors ($\sim$ 80 million) [88]. The large optical bandgap of Si_3N_4, more than three times larger than silicon, allows for neglecting TPA at wavelengths in the telecommunication band. This, together with the low propagation loss, is the key aspect for nonlinear optics. The nonlinear Kerr coefficient however is $\sim 0.2 \cdot 10^{-18}$ m^2/W [26], roughly two orders of magnitude lower than silicon. In Paper F we give a detailed analysis of the optical properties of Si_3N_4.
The main fabrication challenge when depositing thick layers of Si_3N_4 is an increased tensile stress in the film that leads to cracking of the layer above $\sim$ 300 nm [89]. A larger thickness is required for optimal dispersion engineering and light confinement. To overcome this challenge, different strategies have been investigated including thermal cycling [90], PECVD frequency alternation [91], mechanical stress barriers [29, 92] and deposition in trenches [93, 94]. With thin waveguides ($40-50$ nm) the cracking problem is avoided completely and in addition ultra-low propagation loss properties are achieved by reducing the sidewall scattering losses [23] but it is not possible to attain high nonlinear parameters nor low dispersion in this waveguide design. In thick high-confinement waveguides, the nonlinear capability of this material has been shown in experiments like supercontinuum generation [95], harmonic generation in a microring cavity (second-harmonic generation (SHG) and third-harmonic generation (THG)) [96] and resonator based Kerr frequency comb generation [90, 97–99]. In thin waveguides with very low propagation loss FWM-based wavelength conversion has been demonstrated in Paper A. Over all presented platforms the broadest supercontinuum generation (495 THz) [28] has been achieved in stoichiometric silicon nitride as well as coherent octave-spanning microresonator combs [100]. In Paper G we theoretically evaluated the propagation loss that is required to achieve 10 dB signal net-gain in this platform.

Silicon-rich nitride

The variation of the ratio between silicon and nitrogen in non-stoichiometric silicon nitride, Si_xN_y, gives a degree of freedom to change the optical and mechanical properties of the material. This enables for instance modifying the refractive index and optical bandgap between the one achieved for Si_3N_4 and silicon as shown in Paper F. The material with an increased silicon content in comparison to Si_3N_4 is often referred to as silicon-rich nitride. The material brings a relaxation of the tensile stress that is achieved when growing these layers [101, 102], allowing to achieve thick cores in a single deposition step.

A flexible and reliable deposition with variable compositions of Si_xN_y is given within the CMOS fabrication environment explored in detail for LPCVD deposition in Paper F and for PECVD deposition in [103]. Lately, research has been carried out to explore the impact of the composition on the nonlinear Kerr coefficient in more detail. Using PECVD nonlinear Kerr coefficients of $\sim 2 \cdot 10^{-18}$ m^2/W has been reported in [103] and up to $\sim 28 \cdot 10^{-18}$ m^2/W in [104]. Using LPCVD we showed Kerr coefficients of up to $\sim 1.1 \cdot 10^{-18}$ m^2/W in Paper F where we also related the increased nonlinearities to a reduced optical bandgap. The nonlinear performance in silicon-rich nitride has been presented in a FWM experiment in Paper B and supercontinuum generation in Paper C. Furthermore, we demonstrated XPM-based all-optical processing in Paper D and E.

Hydex
Hydex, invented by the company Little Optics, is a high-index doped silica glass with a refractive index between 1.5 and 1.9 (at 1.55 µm wavelength) close to silicon oxynitride. It has a nonlinear Kerr coefficient of $0.1 \cdot 10^{-18}$ m^2/W [105] which is slightly below the one for Si_3N_4. Waveguides with very low propagation loss have been fabricated in this platform, which enables a long effective length. Nonlinear experiments have been performed in order to show the potential of Hydex waveguides for nonlinear optics including FWM [106], wavelength conversion in non-resonant waveguides [107] and microrings [108] as well as supercontinuum [105] and comb generation [109, 110].

4.4 Comparison to HNLF

In order to compare these nonlinear platforms between each other, the maximum achievable nonlinear phase shift $\theta_{\mathrm{nl}} = \gamma P \max L_{\mathrm{eff}}$ (see section 3.5) is calculated. The results will be benchmarked to the HNLF. At the moment HNLF is the best platform for nonlinear optics in terms of maximum nonlinear phase shift. For each platform representative waveguide systems are chosen. The calculations of the nonlinear phase shift are based on the detailed information shown in Table 4.1. Crucial for the calculation of the maximum nonlinear phase shift is the maximum effective length but also the maximum possible power that is launched into the system. For platforms that do not show TPA a reasonable power of 2 W is taken and for HNLF a stimulated Brillouin scattering (SBS) limited maximum power of 500 mW is assumed. In general, the SBS threshold is increased by straining the HNLF, changing its material composition or by modulating the CW pump. For platforms that display TPA the maximum launched power was chosen as the value when the nonlinear TPA loss reaches either 10% (Fig. 4.2.a) or 1% (Fig. 4.2.b) of the linear loss according to Eq. 3.11. The TPA parameter and effective area used

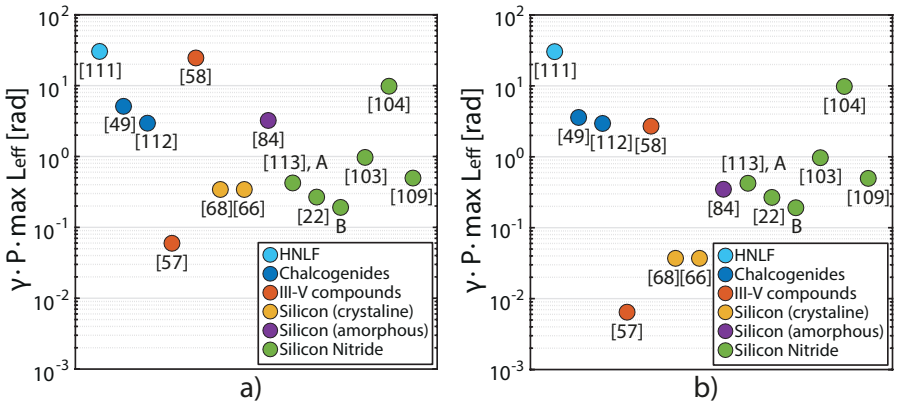

Figure 4.2: (a) Maximum nonlinear phase shift with nonlinear loss restricted to 10% of linear loss. (b) Maximum nonlinear phase shift with nonlinear loss restricted to 1% of linear loss. (The platforms are evaluated according to the parameters provided in Table 4.1.)

for the calculations are provided in Table 4.1. This means that we restrict the analysis to the linear loss regime to simplify the comparison, as max L_{eff} is calculated for all materials as $1/\alpha_{\text{lin}}$. Fig. 4.2.a shows the higher nonlinear phase shift is obtained for chalcogenides, III-V, amorphous silicon and HNLF. Crystalline silicon and silicon nitrides show in general a similar performance. For the more stringent demand in the maximum launched power, the result changes. Still ChGs, AlGaAs and HNLF show the largest nonlinear phase shift. Here, the material suffering from TPA shows worse performance. Silicon nitride becomes better in comparison to silicon and becomes the best CMOS-compatible platform for nonlinear optics. This is a rough estimation of the nonlinear phase shift as three-photon absorption and FCA have not been considered thus resulting in similar performance of silicon with and without p-i-n structure. As shown in Fig. 3.3, the FCA becomes the dominant nonlinear loss contribution at higher power levels. Therefore, a more detailed consideration of the nonlinear absorption effects is required that also accounts for the reduction of nonlinear loss with decaying power. This was done for silicon waveguides as presented in Paper G. The paper shows the impact of TPA and free-carrier lifetime on the nonlinear phase shift and illustrates that there is an optimum power level to maximize the nonlinear performance. In order to implement devices that allow nonlinear operations over a broad bandwidth, the dispersion becomes relevant as discussed before. This point is not included in the discussion but the relevant information about the achieved dispersion

in the presented devices is included in Table 4.1.

4.5 Conclusion

It becomes clear after the presentation and comparison of the material platforms in this chapter, that there is no platform that combines low loss, high nonlinearities and the absence of nonlinear absorption. In distinct platforms, different record performances have been achieved, which indicates that each platform can outperform each other in terms of selected features. To conclude this chapter, the major advantages and disadvantages of each material platform are briefly summarized.
Chalcogenides offer good nonlinear performance. However, the chalcogenide glasses are not CMOS-compatible.
III-V compounds have demonstrated flexibility when it comes to tailoring material properties. Especially AlGaAs combines high refractive index and high nonlinearities, leading to highly efficient nonlinear processes. Missing CMOS-compatibility and the required epitaxial growth brings fabrication disadvantages.
Crystalline silicon has high nonlinearities and is a highly mature (CMOS-compatible) platform with easy access through commercially available SOI-wafers or multi-project wafer runs. Potential for monolithic co-integration with electronic components is another strong advantage of this platform. Nevertheless, crystalline silicon shows nonlinear loss constraints limiting the used power levels, and silicon can not be deposited in crystalline form on top of amorphous wafer substrates like silica.
Amorphous silicon shows high nonlinear Kerr coefficients and the low temperature deposition technique allows for flexible deposition with potential layer stacking. Reported temporal instability is the drawback.
Silicon-rich nitride offers CMOS-compatibility and has the possibility to be deposited flexibly on amorphous substrates. Furthermore low propagation losses are reported within this platform. The moderate nonlinearities and the high tensile stress in thick films are the drawback.
Nonstoichiometric silicon nitride is a CMOS-compatible material and offers flexible processing of thick layers suitable for dispersion engineering. The optical properties of the compound can be engineered by changing the composition of silicon and nitrogen. High propagation losses are the drawback.
Hydex has very low propagation losses. The low nonlinearities and the low refractive index are drawbacks. The platform is not widely available.

Table 4.1: Comparison of material platforms for nonlinear optics regarding the Kerr coefficient n_2, two-photon absorption TPA, effective area A_{eff}, nonlinear parameter γ, propagation loss, group-velocity dispersion (GVD) β_2 and waveguide design. The main reference is given in the last column. Material information taken from other references are marked accordingly.

Platform	Material	n_2 [10^{-18} m^2/W]	TPA α_2 [10^{-15} m/W]	A_{eff} [µm^2]	γ [(W·m)$^{-1}$]	Loss [dB/m]	GVD β_2 [ps^2/m]	design	ref.
HNLF	SiO_2 based	0.026	-	9	0.01	0.0009	zero-GVD at 1541 nm	fiber	[111]
ChGs	$Ge_{11.5}As_{24}Se_{64.5}$	8.6	100	0.24	136	250	-84	strip	[49]
	As_2S_3	2.92	6.2 [44]	7.1	1.7	5	433	rib	[112]
III-V	GaAs	15.9	102 000 [20]	1.8	36	600	n.i.[b]	strip	[57]
	$Al_{0.17}Ga_{0.83}As$	26	300-500 [59]	0.16	660	140	-127	strip	[58]
CMOS-	c-Si (with p-i-n)	4.5 [20]	5 000	0.06	280	100	n.i.[b]	rib	[68]
compatible	c-Si	4.5 [20]	5 000	0.006	360	360	-3445	strip	[66]
materials	a-Si:H	21	2 500	0.07	1 200	45	-0.42	strip	[84]
	Si_3N_4 (low conf.)	0.09 [a]	-	1.28	0.1-0.3	6	0.7	strip	[113],Paper A
	Si_3N_4 (high conf.)	0.26	-	0.88	1.2	40	zero-GVD at 1560 nm	strip	[22]
	Si_xN_y (LPCVD)	0.6	-	0.81	3	140	-77	strip	Paper B
	Si_xN_y (PECVD)	1.6	-	0.4	16	150	n.i.[b]	strip	[103]
	Si_xN_y (PECVD)	28	-	0.23	500	450	n.i.[b]	strip	[104]
	SiON (Hydex)	0.11	-	2	0.2	4	10	strip	[109]

[a] effective n_2 for low-confinement waveguide
[b] no information available in reference

Chapter 5

CMOS-compatible micro- and nanofabrication

To understand the manufacturing processes that enable silicon-based integrated optical systems, in this chapter relevant CMOS-compatible micro- and nanofabrication steps are introduced.

5.1 CMOS-compatible photonics

Electronic components, such as microprocessors, have evolved tremendously in performance during the last decades, while keeping price low and even reducing footprint size. The reasons for this can be found in the development of the micro- and nanofabrication techniques and infrastructure for electronics. Mass production and miniaturization led to a tremendous improvement of integrating functionalities on microchips referred to as integrated circuits (ICs). One key component for integrated logic is the metal-oxide-semiconductor field-effect transistor (MOSFET) which forms the building block for CMOS technology. In general, the term CMOS-compatible defines fabrication techniques and materials that may be used in a CMOS processing line without risk of contamination or other adverse effects. Materials that are compatible with the CMOS fabrication infrastructure benefit from a mature processing platform that offers ideal conditions for low-cost mass production.
The CMOS fabrication infrastructure can be used as leverage to manufacture optical waveguides. With the first silicon-based optical waveguide [10] the path of silicon photonics began [114, 115]. The integration of silicon photonics enables major advantages in communication systems [116]. With modern multi-project wafer runs, the high volume processing of CMOS fabs can be used to give fairly low-cost access to integrated photonic systems [14, 117].

5.2 Ellipsometry

5.2.1 Introduction

Ellipsometry is a widespread measurement technique to characterize material properties of thin films and surfaces in wavelength ranges from the near-UV to the far-IR. Properties like the dielectric function of a material (see 2.1) or the thickness of a deposited film are measured with the ellipsometer in an indirect manner by analyzing the interaction of polarized light with the sample under test.
In detail, the ellipsometer directs a beam of linearly polarized light to the sample where the material changes the polarization state of the light beam that is then detected and analyzed. The relative change in state of polarization, the complex ellipsometer parameter ρ, is described by

$$\rho = tan(\psi)e^{i\delta} \tag{5.1}$$

with ψ and δ as change in magnitude and phase of light before and after the sample. The polarized light is expressed by a superposition of the orthogonal basis vectors p-polarization and s-polarization that allows to define every state of polarization. The interaction of light with matter is theoretically described according to the Fresnel equations yielding two independent complex Fresnel coefficients for light with p-and s-polarization R_p and R_s according to

$$\rho = \frac{R_p}{R_s}. \tag{5.2}$$

The Fresnel equations are based on Snell's Law and include film thickness and refractive indices (complex permittivity, see section 2.1) to define the relative polarization change induced by the material.
In an iterative process the parameters of the Fresnel equations are used as fitting parameters to match the measured ellipsometer parameter described by Eq. 5.1.

5.2.2 Tauc-Lorentz Model

In this work we studied the optical properties of silicon nitride films. For the characterization we performed a simple approach where the silicon nitride was deposited directly on a silicon substrate with known properties. For the silicon nitride film we defined a theoretical model that represents the complex permittivity of the material. It is common to refer to this model as the general oscillator model as it includes the pole information (see Fig. 2.1) as oscillator functions. In the model the complex permittivity is expressed by

$$\epsilon_{\mathrm{r}} = offset + \epsilon_{\mathrm{UV}} + \epsilon_{\mathrm{IR}} + \epsilon_{\mathrm{TL}}, \tag{5.3}$$

where $offset$ is a constant of 1, ϵ_{UV} is the UV pole contribution, ϵ_{IR} the pole contribution at IR frequencies and ϵ_{TL} is the Tauc-Lorentz oscillator term. The first three terms are real functions thus not including material absorption. The Tauc-Lorentz oscillator term is complex and models the material absorption close to the band gap. The three oscillator functions are

$$\begin{aligned} \epsilon_{\mathrm{UV}} &= \frac{A_{\mathrm{UV}}}{E_{\mathrm{UV}}^2 - E^2} \\ \epsilon_{\mathrm{IR}} &= \frac{A_{\mathrm{IR}}}{E_{\mathrm{IR}}^2 - E^2} \\ \epsilon''_{\mathrm{TL}} &= \left[\frac{A_{\mathrm{TL}} E_{\mathrm{TL}} (E - E_{\mathrm{g}})^2}{(E^2 - E_{\mathrm{TL}}^2) + C^2 E^2} \cdot \frac{1}{E} \right]. \end{aligned} \tag{5.4}$$

In the equations, E is the photon energy, A_{xx} and E_{xx} describe the strength and location of the corresponding oscillators, C is a broadening term and E_{g} is the optical bandgap. All these parameters and the thickness of the film are used as fitting parameters to match the ellipsometer measurement data. The shown ϵ''_{TL} in Eq. 5.4 is the imaginary part of the complex dielectric function ϵ_{TL}. The real part is obtained via the Kramers-Kronig relation. For the material characterization carried out in Paper F we used the complete analytical solution of the Kramers-Kronig integral provided in [118].

5.3 Optical lithography

One of the most important manufacturing steps in the environment of semiconductor fabrication is the lithography process. This step combines the reproducible transfer of patterns for dedicated functionality onto the wafer. The patterns are geometries dedicated to produce structures as e.g. electrical contacts, passivation areas, areas for localized doping or etching of ridges, trenches or mesas. It is important to mention that during the lithography step the geometries are only structured and prepared for further processing steps such as etching. Optical lithography offers high throughput and comes with relatively affordable equipment.
In the lithography process the system design is projected via a photomask onto a photosensitive polymer on the wafer. The photomask contains transparent parts (glass) and opaque parts (chromium). As the photomask is aligned in between the light source and wafer (with photoresist), the optical radiation passes through the photomask and exposes only the selected areas of the resist where the photomask is transparent. The photosensitive resist then undergoes a chemical change when exposed to radiation. An example of the exposure step during the lithography process is illustrated in Fig. 5.1.a. Light sources used for optical lithography are in the regime of UV, deep ultraviolet (DUV)

or extreme ultraviolet (EUV), reaching wavelengths from 400 nm down to around 100 nm. The resolution in terms of the minimum feature size that can be exposed scales with wavelength. In the case of optical contact lithography where photomask and wafer are in contact, the minimum resolved feature is described by [64]

$$W_{min} \approx \sqrt{k\lambda g}, \tag{5.5}$$

where λ is the wavelength, k is the resist specific technology parameter (often around 1) and g is the gap between photomask and wafer. As an example, a gap of 2 µm and a light source with 300 nm wavelength would give a minimum feature size of around 800 nm. In the case of projection lithography the minimal feature size is described by [64]

$$W_{min} \approx k\frac{\lambda}{\mathrm{NA}}. \tag{5.6}$$

Here an objective with a numerical aperture (NA) is placed between the mask and wafer in order to project a smaller image of the mask onto the wafer and achieve a scaling down of the mask geometries. The use of optical projection lithography at 193 nm wavelength is the standard in industry and waveguide fabrication has been reported in [43]. Both equations show that lithography using shorter wavelengths yields a smaller minimum feature size that can be resolved during exposition. After exposure the photoresist is developed where exposed parts are removed for positive photoresists, while unexposed parts are removed for negative photoresists. The exposing radiation activates a different photosensitive chemistry in positive and negative resists. In positive resist the radiation triggers a scission of polymer chains leading to the reduction of its molecular weight that makes it easier to be resolved during development. The opposite effect takes place in a negative resist where cross polymerization leads to a reduced dissolution behavior. The remaining resist structures can serve as an etchmask or define openings for other processing steps like metal deposition with lift-off. The developed positive photoresist of the lithography example is illustrated in Fig. 5.1.b.

Higher resolution than optical lithography can be achieved using electron-beam (ebeam) lithography. A shorter wavelength compared to optical radiation is achieved by the acceleration of electrons to high energies. Electron-sensitive resist is exposed by a focused electron beam. This technique is used to create photomasks or write masks directly on the wafer for very small features. Although writing features well below 100 nm are possible [64], the ebeam lithography has a serial writing procedure making the process time consuming, and the equipment is expensive and complex. This lithography technology is therefore unsuitable for mass production and in that sense not CMOS compatible.

The fabrication processes utilized in Papers A−F make use of optical contact

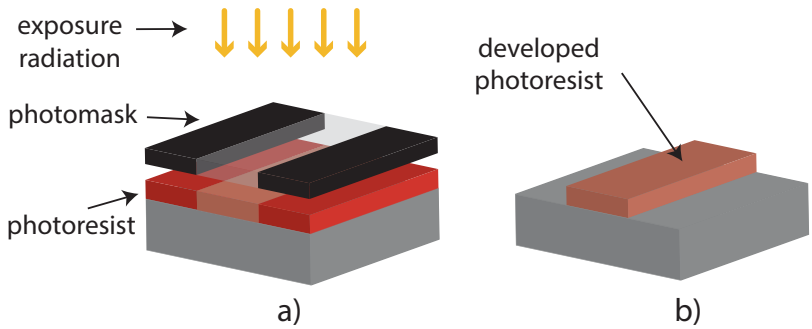

Figure 5.1: Illustration of optical lithography a) Illustration of the exposure process. The dark areas of the photomask are opaque. The bright area of the photomask is transparent for the exposure radiation. b) Illustration of the developed positive photoresist after exposure.

lithography. In Papers B–F a DUV-light source with a wavelength around 220 nm was used and openings of below 400 nm were resolved completely after the lithography and etching processes.

5.4 Thermal oxidation

The success of silicon as the primary semiconductor material in the field of electronics is based on its high-quality oxide [64]. A low amount of defects and an easy fabrication process makes the combination of silicon and silicon dioxide a powerful alliance in integrated circuits with fast switching MOSFETs with low power consumption. The oxide is formed during an oxidation process in which silicon undergoes a chemical reaction with oxygen in order to create silicon dioxide according to [64]

$$\mathrm{Si(solid)} + \mathrm{O_2(gas)} \longrightarrow \mathrm{SiO_2}\,. \tag{5.7}$$

It is important to mention that the oxidation reaction only takes place at the silicon surface. As a layer of SiO_2 builds up on top of the silicon wafer, oxygen atoms have to diffuse through the oxide layer in order to react at the silicon surface to form the SiO_2. At room temperature a silicon wafer oxidizes by only 2.5 nm and further oxidation is halted as the mobility of oxygen atoms is too low to diffuse through the oxide layer. Therefore thermal oxidation is carried out at process temperatures around $700 - 1\,200°C$ for increased diffusion of oxygen towards the silicon surface. Silicon oxidation is commonly done under atmospheric pressure (760 Torr) and a distinction

is made between dry oxidation with molecular oxygen (O_2) as oxidant and wet oxidation with water vapor (H_2O) as oxidant. Dry oxidation has the advantage of a denser oxide with higher quality whereas in wet oxidation a higher oxidation rate is achieved. The oxidation reaction takes place at the interface between silicon and silicon dioxide. Gaseous water molecules have to diffuse from the wafer environment through the silicon dioxide to reach the interface. The oxidation rate becomes important when growing thick oxides as the rate decreases significantly with increasing oxide thickness. The increased oxidation rate in the wet oxidation compared to dry oxidation comes from the higher diffusivity of H_2O through the oxide layer in comparison with O_2. The difference in rate becomes clear when oxidizing a 1 µm layer of SiO_2 as dry oxidation takes 48 hours while wet oxidation takes 2 hours. In optical waveguide systems, typical oxide thicknesses of around $1 - 4$ µm are used in order to avoid leakage of light from the waveguide to the substrate. In the fabrication processes of Papers A−F thermal wet oxidation was used. An oxide around 3 µm was grown in Papers B−F where high confinement waveguides were fabricated. For the unconventional low confinement waveguide presented in Paper A an oxide thickness of 15 µm was grown in order to avoid substrate leakage [23].

5.5 Thin-film deposition

In order to deposit thin films of dedicated materials, several deposition techniques are available in the CMOS library of micro- and nanofabrication. The principle of all techniques is based on the transition of materials from a molecular movable state (gaseous or liquid) to the solid state to form a deposition on top of a wafer substrate. To prepare molecules for precipitation on a substrate, physical or chemical reactions can be utilized. Common physical deposition processes are evaporation and sputtering where the vaporized material condensates on a substrate. Vaporization of the deposition material is done by thermal heating of the source (evaporation) or by energetic ion bombardment (sputtering). A thin-film deposition technique based on chemical reactions is called chemical vapor deposition (CVD). In the CVD process gaseous chemicals react at the wafer surface to start a chemical deposition process. The activation energy for the chemical reaction to happen is commonly thermal or plasma assisted, naming the CVD process either low-pressure chemical vapor deposition (LPCVD) or plasma-enhanced chemical vapor deposition (PECVD).

5.5.1 LPCVD

In LPCVD processes the chemical reaction is driven by temperature. Typical temperature values in the LPCVD reaction chamber are around $700 - 800°C$.

The atomic composition of the precursor gases pumped into the reaction chamber defines the material composition of the deposited film. Changing the gas flow of the individual precursor gases can change the atomic composition of the deposit. This also enables *in-situ* doping of films by adding other gaseous chemicals. The precursor gases are introduced into the reaction chamber in non-reactive form and start to decompose once reaching the hot substrate region in the reactor where the decomposed reaction products are deposited. The benefit of having a low pressure in the chamber of around $0.1-1.0$ Torr is that gas phase nucleation is minimized resulting in formation of solid clusters of atoms only on the wafer surface. This leads to a high uniformity of the deposited film. Two different types of reactors are used, cold-wall and hot-wall reactors. In cold-wall reactors the deposition reaction only takes place at the surface of the wafer. Hot-wall reactors on the other hand have a more uniform distribution of temperature and reduced convection effects, but a film is deposited at the reactor wall leading to a memory effect of the chamber. Common materials deposited with LPCVD are silicon nitrides and silicon dioxide. In the manufacturing process of Papers A−F the deposition of silicon nitride was done using LPCVD.

5.5.2 PECVD

The primary nonthermal energy source which is used to drive a CVD-based process is the radio-frequency (RF) plasma. Therefore the PECVD process offers the advantage of distinct reduction of process temperatures in comparison to LPCVD. Typical deposition temperatures for PECVD processes are around $200-400°C$. These fairly low temperatures feature an increased substrate protection and allow film deposition on top of temperature-critical substrates (e.g. metalization layers). Common materials for deposition in a PECVD system are silicon-based oxides and nitrides that are mainly used for passivation. Furthermore, the RF power of the plasma is an additional parameter that offers control over the deposited film properties.

5.5.3 Silicon nitride deposition by LPCVD and PECVD

The deposition of silicon nitride as a material for waveguide cores has been shown in both LPCVD [119] and PECVD [26] processes. The film quality of LPCVD nitride is in general higher compared to a PECVD nitride. This comes from the $15-30\%$ higher hydrogen content in PECVD nitrides resulting in larger optical absorption at telecom wavelengths [120]. The stress in thick films of deposited stoichiometric silicon nitride (indicated in section 4.3.2) used for optical waveguides and micro-electro-mechanical systems (MEMS) devices [121] can give rise to cracks in the layers. One approach to avoid film cracks is to change the content of silicon and nitrogen from stoichiometric (Si_3N_4)

to silicon enriched. This has been shown with LPCVD in Papers B−F and [101] and also with PECVD in [122]. Another alternative to reduce the film stress in silicon nitride film is by depositing different layers at alternating RF frequencies of the plasma [91, 123, 124].

5.6 Reactive ion etching

To transfer the pattern from an etch mask into the substrate, an etching procedure is required. In general, etching can be carried out in dry or wet form. Wet etching is mostly isotropic[1] and performed in an etch bath where the pure chemical process can offer a high etch selectivity between materials. Dry etching on the other hand provides an anisotropic etch. This enables better control over the process in comparison to wet etching because there are more available process parameters in dry etching. One special form of dry etching is ion milling where ionized molecules are accelerated in an electric field towards the target substrate. The bombardment of ions with high kinetic energy towards the wafer surface leads to the constant sputtering of surface molecules. This pure physical process has the advantage of a high degree of anisotropy, but typically has low selectivity [64].
A dry etching process that can provide both selectivity and anisotropy simultaneously is reactive-ion etching (RIE) by supporting both chemical and physical etching properties. RIE is commonly used to etch silicon-based materials (e.g. Si, SiO_2, Si_xN_y) with halogen-based etch-chemicals (e.g. CHF_3, CF_4). The physical component of the etching comes from electric-field-assisted acceleration of ionized species toward the surface of the wafer similar to the ion milling process. The chemical component comes from the gaseous etching chemicals used in the process that are ionized and broken down by the plasma inside the etch chamber to form chemically reactive species. The radical species undergo a chemical reaction and break the bonds of surface atoms on the wafer. In this process the binding of surface atoms to reactive radicals becomes energetically favored so that volatile reaction products are formed that are exhausted from the etching chamber. The chosen carbon containing etch chemicals leave reaction by-products like carbon that form polymer coatings on the wafer. This carbon deposition is removed by physical collisions with incident ions. As the impact of ions is lower on vertical sidewalls, the polymer sidewall passivation assists anisotropic etching. In Papers B−F the etching of the silicon nitride layers was performed in an RIE process.

[1] An isotropic etching process is characterized by the same etching speed in all directions. Exception for this etch behavior is the wet etching in materials like silicon where the etching can be directed by the crystal planes allowing to wet etch in anisotropic manner.

Chapter 6

Future outlook

As presented in Paper G, in order to realize parametric signal net-gain of ∼10 dB, propagation losses of 0.05 dB/cm are required in a silicon nitride waveguide. In comparison to this value, our present waveguides fabricated from Si_3N_4 show losses of around 0.4 dB/cm (Paper F). Thus, in order to reach the net-gain target, a further reduction of the propagation losses are necessary. The recommended changes of our established fabrication process that may lead to a reduction of the waveguide propagation losses are the following:
In Paper B, we estimated losses occurring from the scattering at the waveguides sidewalls to be around 0.2 dB/cm. In order to reduce these losses, it is essential to minimize the roughness of the core sidewalls. Assuming that the roughness is translated from the etch mask, it is required to improve the existing lithography process. One option for improvement is to study the reflow properties of the resist at different temperatures during the hardbake step. The temperature is to be optimized so that the best resist smoothness is achieved.
In Paper F, we reported the increase of waveguide propagation losses for silicon nitride compositions with increased silicon content. The loss measurements were carried out in the wavelength range between 1510 and 1610 nm. However, according to the ellipsometer measurements, we estimated material transparency for all compositions at wavelengths above 600 nm. This discrepancy may originate from increased material scattering in the material. It was observed throughout this work that a reduction in furnace pressure led to a reduction in propagation loss for the silicon rich nitride compositions. One potential explanation is the relation between furnace pressure and gas phase nucleation [64] that could be related to increased material scattering. Knowledge about the correlation between the furnace pressure and the propagation

losses could lead to loss improvements in all silicon nitride compositions.

Chapter 7

Summary of papers

Paper A

"Continuous wave-pumped wavelength conversion in low-loss silicon nitride waveguides," *Optics Letters*, vol. 40, no. 6, pp. 875-878, March 2015.

This paper presents the linear and nonlinear characterization of low-loss low-confinement waveguides fabricated from stoichiometric silicon nitride. These waveguides were fabricated by the group of John Bowers (University of California Santa Barbara). The 100 nm thin waveguide core leads to low optical confinement and results in low propagation loss of 0.06 dB/cm. In a nonlinear FWM experiment, wavelength conversion 10 Gb/s OOK data has been demonstrated. This paper shows that a similar conversion efficiency to SOI waveguides could be achieved with Si_3N_4, despite the inherently lower nonlinear coefficient.

My contribution: This experimental work was performed in joint collaboration with the group of John Bowers at UCSB, which provided the waveguides. At Chalmers I developed and built the measurement environment for the waveguide characterization, prepared and performed the measurements. I implemented and performed the simulations. I presented the results at CLEO 2014 and wrote the first draft of the paper.

Paper B

"Linear and nonlinear characterization of low-stress high-confinement silicon-rich nitride waveguides," *Optics Express*, vol. 23, no. 20, pp. 25828-25837, Sept. 2015 + **Erratum,** *Optics Express*, vol. 25, no. 7, pp. 7443-7444, April 2017.

This paper presents the fabrication, simulation and characterization of high-confinement waveguides based on non-stoichiometric silicon nitride. This waveguide platform was developed at Chalmers. The propagation and coupling losses have been shown in a wavelength-resolved manner and the contribution of the scattering loss evaluated. In mode-solver simulations the dispersion and confinement properties in terms of the waveguides dimensions has been studied. Nonlinear FWM experiments has been shown and the functionality of a microring resonator has been presented, displaying high-quality factors $\sim 10^5$ in the 1.5 µm wavelength regime. We showed that this platform has similar nonlinear performance compared to Si_3N_4 with the additional advantage of a high yield fabrication process.

My contribution: I developed the waveguide fabrication process and performed the complete waveguide fabrication. I expanded the previously implemented measurement environment for waveguide characterization and developed the wavelength-resolved loss measurement technique. I prepared and performed the measurements. I assisted in developing the mode solver and performed parts of the simulations. I presented the results at OFC 2015 and wrote the first draft of the paper.

Erratum: In the erratum we corrected the measured nonlinear Kerr coefficient. The mistake originated from underestimating the coupled power in the dual-pump experiment. The correction does not impact the conclusions drawn in the paper.

Paper C

"Octave-spanning supercontinuum generation in a silicon-rich nitride waveguide," *Optics Letters*, vol. 41, no. 12, pp. 2719-2722, June 2016.

In this paper we use the high-confinement silicon-rich nitride waveguides to generate a more than octave-spanning supercontinuum. The experiments were conducted by the group of Morten Bache (DTU) using the waveguides developed and fabricated at Chalmers. The supercontinuum was generated from sub-kW 130 fs pulses. The results demonstrate that this platform enables sim-

ilar nonlinear performance as low-loss stoichiometric silicon nitride waveguide with the direct advantage of having a simplified fabrication process.

My contribution: I contributed to the waveguide design and performed the waveguide fabrication. I conducted the material characterization that provided the information for the waveguide simulations. I assisted in writing the paper.

Paper D

"Cross-phase-modulation-based wavelength conversion in low-stress silicon-rich nitride waveguide," *Optical Fiber Communication Conference (OFC)*, Anaheim, USA, paper Tu2K.4, March 2016.

In this paper we showed all optical signal processing based on cross-phase modulation. The experiments were performed by the group of Lawrence Chen (McGill University) using the waveguides developed and fabricated at Chalmers.The dimensions of the waveguides were engineered in order to achieve flat anomalous dispersion across the C- and L-band.
The performed interferometer-based measurements confirmed the simulated dispersion values. With the dispersion engineered waveguides we showed ultra-broad band wavelength conversion based on XPM. The broad-band nonlinear performance was demonstrated by wavelength conversion of 10 Gb/s RZ-OOK data across the C-band.

My contribution: I contributed to the waveguide design and performed the waveguide fabrication. I conducted the material characterization that provided the required parameters for the waveguide simulations. I assisted in writing the paper.

Paper E

"All-optical radio frequency spectrum analyzer based on cross-phase modulation in a silicon-rich nitride waveguide," *IEEE International Topical Meeting on Microwave Photonics (MWP)*, Long Beach, USA, paper ThM1.5, Nov. 2016.

In this paper we demonstrated an all optical radio frequency spectrum analyzer based on cross-phase modulation. This work was carried out in collaboration with the group of Lawrence Chen at McGill University using the waveguide fabricated at Chalmers University. We explored XPM-based spectral broadening of a cw probe to analyze the RF spectrum of the intensity-modulated signal in the optical domain. In the dispersion engineered waveguides we mea-

sured the bandwidth of the RFSA to be above 560 GHz. In experiments we demonstrated the performance of this all-optical spectrum analyzer with resolved spectral characterization of modulation rates up to 160 GHz.

My contribution: I contributed to the waveguide design and performed the waveguide fabrication. I assisted in writing the paper.

Paper F

"Optical bandgap engineering in nonlinear silicon nitride waveguides," *Submitted*, March 2017.

This paper presents the impact of the silicon nitride composition of a high-confinement waveguides on its linear and nonlinear properties. With a focus on low-pressure chemical vapor deposition (LPCVD) it was shown how the gas flow ratio during deposition serves as a way to change optical and mechanical properties of the material. Measurements of linear loss and material-specific nonlinear Kerr coefficients were carried out for five silicon nitride composition ranging from stoichiometric (Si_3N_4) to silicon-rich. In mode-solver simulations waveguide geometries were presented that led to desired anomalous group-velocity dispersion and increased nonlinearities. The measured nonlinear Kerr coefficient of the five compositions was compared with theoretical expectations and other platforms for nonlinear integrated optics. This was the first holistic characterization of the nonlinear performance of LPCVD silicon nitride for various compositions.

My contribution: I expanded the previously developed fabrication process and performed the fabrication of the waveguides. I implemented the ellipsometer model for the silicon nitride film characterization. I conducted the mode solver simulations. I presented the results at OFC 2017 and wrote the paper with support from the co-authors.

Paper G

"Towards on-chip net-gain in CMOS-compatible waveguides," *CLEO-Europe*, Munich, Germany, June 2017.

In this work we theoretically discuss performance requirements to achieve 10 dB on-chip net-gain in three popular CMOS-compatible platforms for nonlinear integrated optics. We discussed the material platforms silicon nitride (Si_3N_4) and silicon (c-Si) where the silicon waveguide also included a hypo-

thetical waveguide design with carrier removal. We highlighted the relevant tuning parameters in all three platforms in order to maximize the achievable nonlinear phase shift. This study sets benchmark requirements to reach the targeted 10 dB net-gain on chip.

My contribution: I implemented and performed the numerical simulations. I wrote the paper with support from the co-authors.

Bibliography

[1] K. C. Kao and G. A. Hockham, "Dielectric-fibre surface waveguide for optical frequencies," *Procedings of the IEE*, vol. 113, no. 7, pp. 1151–1158, 1966.

[2] D. A. B. Miller, "Optical interconnects to silicon," *IEEE Journal on Selected Topics in Quantum Electronics*, vol. 6, no. 6, pp. 1312–1317, 2000.

[3] J. W. Goodman, F. J. Leonberger, S.-Y. Kung, and R. A. Athale, "Optical interconnections for VLSI systems," *Proceedings of the IEEE*, vol. 72, no. 7, pp. 850–866, 1984.

[4] A. Alduino and M. Paniccia, "Interconnects: Wiring electronics with light," *Nature Photonics*, vol. 1, no. 3, pp. 153–155, 2007.

[5] J. A. Tatum, D. Gazula, L. A. Graham, J. K. Guenter, R. H. Johnson, J. King, C. Kocot, G. D. Landry, I. Lyubomirsky, A. N. MacInnes, E. M. Shaw, K. Balemarthy, R. Shubochkin, D. Vaidya, M. Yan, and F. Tang, "VCSEL-based interconnects for current and future data centers," *Journal of Lightwave Technology*, vol. 33, no. 4, pp. 727–732, 2015.

[6] A. Larsson, "Advances in VCSELs for communication and sensing," *IEEE Journal of Selected Topics in Quantum Electronics*, vol. 17, no. 6, pp. 1552–1567, 2011.

[7] M. Chacinski, N. Chitica, S. Molin, N. Lalic, and O. Sahlén, "25.78 Gbps data transmission with 850 nm multimode VCSEL packaged in QSFP form factor module," *Optical Fiber Communication Conference and Exposition and the National Fiber Optic Engineers Conference OW1B.1*, 2013.

[8] S. Meister, M. Grehn, H. Rhee, M. Vitali, C. Theiss, S. Kupijai, A. Al-Saadi, D. Bronzi, S. Otte, M. Henniges, D. Selicke, M. Atif, E. Schwartz,

S. Lischke, D. Stolarek, A. Mai, M. Kaynak, H. H. Richter, and L. Zimmermann, "Silicon photonics for 100 Gbit/s intra-data center optical interconnects," *Proceedings of SPIE*, vol. 9753, pp. 975308–7, 2016.

[9] D. Mahgerefteh, C. Thompson, C. Cole, G. Denoyer, T. Nguyen, I. Lyubomirsky, C. Kocot, and J. Tatum, "Techno-economic comparison of silicon photonics and multimode VCSELs," *Optical Fiber Communication Conference M3B.2*, 2015.

[10] R. A. Soref and J. P. Lorenzo, "All-silicon active and passive guided-wave components for $\lambda = 1.3$ and 1.6 µm," *IEEE Journal on Selected Topics in Quantum Electronics*, vol. QE-22, no. 6, pp. 873–879, 1986.

[11] U. Fischer, T. Zinke, J.-R. Kropp, F. Arndt, and K. Petermann, "0.1 dB/cm waveguide losses in single-mode SOI rib waveguides," *IEEE Photonics Technology Letters*, vol. 8, no. 5, pp. 647–648, 1996.

[12] M. J. R. Heck, H.-W. Chen, A. W. Fang, B. R. Koch, D. Liang, H. Park, M. N. Sysak, and J. E. Bowers, "Hybrid silicon photonics for optical interconnects," *IEEE Journal of Selected Topics in Quantum Electronics*, vol. 17, no. 2, pp. 333–346, 2011.

[13] Z. Wang, B. Tian, M. Pantouvaki, W. Guo, P. Absil, J. Van Campenhout, C. Merckling, and D. Van Thourhout, "Room temperature InP DFB laser array directly grown on (001) silicon," *Nature Photonics*, vol. 9, no. 12, pp. 837–842, 2015.

[14] M. Hochberg and T. Baehr-Jones, "Towards fabless silicon photonics," *Nature Photonics*, vol. 4, no. 8, pp. 492–494, 2010.

[15] J. Leuthold, C. Koos, and W. Freude, "Nonlinear silicon photonics," *Nature Photonics*, vol. 4, no. 8, pp. 535–544, 2010.

[16] R. Salem, M. A. Foster, A. C. Turner, D. F. Geraghty, M. Lipson, and A. L. Gaeta, "Signal regeneration using low-power four-wave mixing on silicon chip," *Nature Photonics*, vol. 2, no. 1, pp. 35–38, 2007.

[17] M. A. Foster, A. C. Turner, R. Salem, M. Lipson, and A. L. Gaeta, "Broad-band continuous-wave parametric wavelength conversion in silicon nanowaveguides," *Optics Express*, vol. 15, no. 20, pp. 12949–12958, 2007.

[18] I.-W. Hsieh, X. Chen, X. Liu, J. I. Dadap, N. C. Panoiu, C.-Y. Chou, F. Xia, W. M. Green, Y. A. Vlasov, and R. M. Osgood, Jr., "Supercontinuum generation in silicon photonic wires," *Optics Express*, vol. 15, no. 23, pp. 15242–15249, 2007.

[19] A. D. Bristow, N. Rotenberg, and H. M. van Driel, "Two-photon absorption and Kerr coefficients of silicon for 850-2200 nm," *Applied Physics Letters*, vol. 90, no. 19, pp. 191104–3, 2007.

[20] M. Dinu, F. Quochi, and H. Garcia, "Third-order nonlinearities in silicon at telecom wavelengths," *Applied Physics Letters*, vol. 82, no. 18, pp. 2954–2956, 2003.

[21] J. Bauer, "Optical properties, band gap, and surface roughness of Si_3N_4," *Physica Status Solidi (a)*, vol. 39, no. 2, pp. 411–418, 1977.

[22] D. J. Moss, R. Morandotti, A. L. Gaeta, and M. Lipson, "New CMOS-compatible platforms based on silicon nitride and Hydex for nonlinear optics," *Nature Photonics*, vol. 7, no. 8, pp. 597–607, 2013.

[23] J. F. Bauters, M. J. R. Heck, D. D. John, J. S. Barton, C. M. Bruinink, A. Leinse, R. G. Heideman, D. J. Blumenthal, and J. E. Bowers, "Planar waveguides with less than 0.1 dB/m propagation loss fabricated with wafer bonding," *Optics Express*, vol. 19, no. 24, pp. 24090–24101, 2011.

[24] A. Z. Subramanian, P. Neutens, A. Dhakal, R. Jansen, T. Claes, X. Rottenberg, F. Peyskens, S. Selvaraja, P. Helin, B. Dubois, K. Leyssens, S. Severi, P. Deshpande, R. Baets, and P. Van Dorpe, "Low-loss single-mode PECVD silicon nitride photonic wire waveguides for 532-900 nm wavelength window fabricated within a CMOS pilot line," *IEEE Photonics Journal*, vol. 5, no. 6, p. 2202809, 2013.

[25] R. Heideman, M. Hoekman, and E. Schreuder, "TriPleX-based integrated optical ring resonators for lab-on-a-chip and environmental detection," *IEEE Journal on Selected Topics in Quantum Electronics*, vol. 18, no. 5, pp. 1583–1596, 2012.

[26] K. Ikeda, R. E. Saperstein, N. Alic, and Y. Fainman, "Thermal and Kerr nonlinear properties of plasma-deposited silicon nitride/ silicon dioxide waveguides," *Optics Express*, vol. 16, no. 17, pp. 12987–12994, 2008.

[27] Y. Okawachi, K. Saha, J. S. Levy, Y. H. Wen, M. Lipson, and A. L. Gaeta, "Octave-spanning frequency comb generation in a silicon nitride chip," *Optics Letters*, vol. 36, no. 17, pp. 3398–3400, 2011.

[28] J. P. Epping, T. Hellwig, M. Hoekman, R. Mateman, A. Leinse, R. G. Heideman, A. van Rees, P. J. van der Slot, C. J. Lee, C. Fallnich, and K.-J. Boller, "On-chip visible-to-infrared supercontinuum generation with more than 495 THz spectral bandwidth," *Optics Express*, vol. 23, no. 15, pp. 19596–19604, 2015.

[29] K. Luke, A. Dutt, C. B. Poitras, and M. Lipson, "Overcoming Si_3N_4 film stress limitations for high quality factor ring resonators," *Optics Express*, vol. 21, no. 19, pp. 22829–22833, 2013.

[30] G. P. Agrawal, *Nonlinear Fiber Optics*. Academic Press, 5th ed., 2013.

[31] M. C. Petty, *Molecular Electronics*. Intersience, 2007.

[32] M. Sheik-Bahae, D. J. Hagan, and E. W. Van Stryland, "Dispersion and band-gap scaling of the electronic Kerr effect in solids associated with two-photon absorption," *Physical Review Letters*, vol. 65, no. 1, pp. 96–99, 1990.

[33] R. W. Boyd, *Nonlinear Optics*. Academic Press, 1992.

[34] B. E. A. Saleh and M. C. Teich, *Fundamentals of Photonics*. Interscience, 2nd ed., 2007.

[35] C. Koos, L. Jacome, C. Poulton, J. Leuthold, and W. Freude, "Nonlinear silicon-on-insulator waveguides for all-optical signal processing," *Optics Express*, vol. 15, no. 10, pp. 5976–5990, 2007.

[36] C.-L. Chen, *Foundations for guided-wave optics*. John Wiley & Sons, Inc., 2007.

[37] W. D. Sacher, Y. Huang, G.-Q. Lo, and J. K. S. Poon, "Multilayer silicon nitride-on-silicon integrated photonic platforms and devices," *Journal of Lightwave Technology*, vol. 33, no. 4, pp. 901–910, 2015.

[38] M. R. Watts, H. A. Haus, and E. P. Ippen, "Integrated mode-evolution-based polarization splitter," *Optics Letters*, vol. 30, no. 9, pp. 967–969, 2005.

[39] J. F. Bauters, M. J. R. Heck, D. Dai, J. S. Barton, D. J. Blumenthal, and J. E. Bowers, "Ultralow-loss planar Si_3N_4 waveguide polarizers," *IEEE Photonics Journal*, vol. 5, no. 1, p. 6600207, 2013.

[40] C. Li, J. H. Song, J. Zhang, H. Zhang, S. Chen, M. Yu, and G. Q. Lo, "Silicon polarization independent microring resonator-based optical tunable filter circuit with fiber assembly," *Optics Express*, vol. 19, no. 16, pp. 15429–15437, 2011.

[41] R. G. Hunsperger, *Integrated Optics*. Springer-Verlag, 4th ed., 1995.

[42] J. Lacey and F. Payne, "Radiation loss from planar waveguides with random wall imperfections," *IEE Proceedings*, vol. 137, no. 4, pp. 282–288, 1990.

[43] S. K. Selvaraja, P. Jaenen, W. Bogaerts, D. Van Thourhout, P. Dumon, and R. Baets, "Fabrication of photonic wire and crystal circuits in silicon-on-insulator using 193-nm optical lithography," *Journal of Lightwave Technology*, vol. 27, no. 18, pp. 4076–4083, 2009.

[44] B. J. Eggleton, B. Luther-Davies, and K. Richardson, "Chalcogenide photonics," *Nature Photonics*, vol. 5, no. 3, pp. 141–148, 2011.

[45] A. Gajda, L. Zimmermann, M. Jazayerifar, G. Winzer, H. Tian, R. Elschner, T. Richter, C. Schubert, B. Tillack, and K. Petermann, "Highly efficient CW parametric conversion at 1550 nm in SOI waveguides by reverse biased p-i-n junction," *Optics Express*, vol. 20, no. 12, pp. 13100–13107, 2012.

[46] M. Itoh, T. Saida, Y. Hida, M. Ishii, Y. Inoue, Y. Hibino, and A. Sugita, "Large reduction of singlemode-fibre coupling loss in 1.5% planar lightwave circuits using spot-size converters," *Electronics Letters*, vol. 38, no. 2, pp. 72–74, 2002.

[47] D. Taillaert, P. Bienstman, and R. Baets, "Compact efficient broadband grating coupler for silicon-on-insulator waveguides," *Optics Letters*, vol. 29, no. 23, pp. 2749–2751, 2004.

[48] W. S. Zaoui, A. Kunze, W. Vogel, M. Berroth, J. Butschke, F. Letzkus, and J. Burghartz, "Bridging the gap between optical fibers and silicon photonic integrated circuits," *Optics Express*, vol. 22, no. 2, pp. 1277–1286, 2014.

[49] X. Gai, S. Madden, D.-Y. Choi, D. Bulla, and B. Luther-Davies, "Dispersion engineered $Ge_{11.5}As_{24}Se_{64.5}$ nanowires with a nonlinear parameter of 136 $W^{-1}m^{-1}$ at 1550 nm," *Optics Express*, vol. 18, no. 18, pp. 18866–18874, 2010.

[50] A. Prasad, C.-j. Zha, R.-p. Wang, A. Smith, S. Madden, and B. Luther-Davies, "Properties of $Ge_xAs_ySe_{1-x-y}$ glasses for all-optical signal processing," *Optics Express*, vol. 16, no. 4, pp. 2804–2815, 2008.

[51] M. R. Lamont, B. Luther-Davies, D.-Y. Choi, S. Madden, and B. J. Eggleton, "Supercontinuum generation in dispersion engineered highly nonlinear ($\gamma = 10$ /W/m) As_2S_3 chalcogenide planar waveguide," *Optics Express*, vol. 16, no. 19, pp. 14938–14944, 2008.

[52] R. Neo, J. Schröder, Y. Paquot, D.-y. Choi, S. Madden, B. Luther-Davies, and B. J. Eggleton, "Phase-sensitive amplification of light in a $\chi^{(3)}$ photonic chip using a dispersion engineered chalcogenide ridge waveguide," *Optics Express*, vol. 21, no. 7, pp. 7926–7933, 2013.

[53] M. R. E. Lamont, B. Luther-Davies, D.-Y. Choi, S. Madden, X. Gai, and B. J. Eggleton, "Net-gain from a parametric amplifier on a chalcogenide optical chip," *Optics Express*, vol. 16, no. 25, pp. 20374–20381, 2008.

[54] M. R. E. Lamont, V. G. Ta'eed, M. A. F. Roelens, D. J. Moss, B. J. Eggleton, D.-Y. Choi, S. Madden, and B. Luther-Davies, "Error-free wavelength conversion via cross-phase modulation in 5 cm of As_2S_3 chalcogenide glass rib waveguide," *Electronics Letters*, vol. 43, no. 17, pp. 16–17, 2007.

[55] F. Luan, M. D. Pelusi, M. R. E. Lamont, D.-Y. Choi, S. Madden, B. Luther-Davies, and B. J. Eggleton, "Dispersion engineered As_2S_3 planar waveguides for broadband four-wave mixing based wavelength conversion of 40 Gb/s signals," *Optics Express*, vol. 17, no. 5, pp. 3514–3520, 2009.

[56] V. G. Ta'eed, M. Shokooh-Saremi, L. Fu, D. J. Moss, M. Rochette, I. C. M. Littler, B. J. Eggleton, Y. Ruan, and B. Luther-Davies, "Integrated all-optical pulse regenerator in chalcogenide waveguides," *Optics Letters*, vol. 30, no. 21, pp. 2900–2902, 2005.

[57] W. Astar, P. Apiratikul, T. E. Murphy, and G. M. Carter, "Wavelength conversion of 10-Gb/s RZ-OOK using filtered XPM in a passive GaAs-AlGaAs waveguide," *IEEE Photonics Technology Letters*, vol. 22, no. 9, pp. 637–639, 2010.

[58] M. Pu, L. Ottaviano, E. Semenova, and K. Yving, "Efficient frequency comb generation in AlGaAs-on-insulator," *Optica*, vol. 3, no. 8, pp. 823–826, 2016.

[59] P. Apiratikul, J. J. Wathen, G. A. Porkolab, B. Wang, L. He, T. E. Murphy, and C. J. K. Richardson, "Enhanced continuous-wave four-wave mixing efficiency in nonlinear AlGaAs waveguides," *Optics Express*, vol. 22, no. 22, pp. 26814–26824, 2014.

[60] C. Lacava, V. Pusino, P. Minzioni, M. Sorel, and I. Cristiani, "Nonlinear properties of AlGaAs waveguides in continuous wave operation regime," *Optics Express*, vol. 22, no. 5, pp. 5291–5298, 2014.

[61] P. P. Absil, J. V. Hryniewicz, B. E. Little, P. S. Cho, R. A. Wilson, L. G. Joneckis, and P.-T. Ho, "Wavelength conversion in GaAs micro-ring resonators," *Optics Letters*, vol. 25, no. 8, pp. 554–556, 2000.

[62] M. Pu, H. Hu, L. Ottaviano, E. Semenova, D. Vukovic, L. Oxenløwe, and K. Yvind, "AlGaAs-on-insulator nanowire with 750 nm FWM bandwidth, -9 dB CW conversion efficiency, and ultrafast operation enabling

record Tbaud wavelength conversion," *Optical Fiber Communication Conference Th5A.3*, 2015.

[63] M. Pu, L. Ottaviano, E. Semenova, L. K. Oxenløwe, and K. Yvind, "Ultra-Low threshold power on-chip optical parametric oscillation in AlGaAs-On-Insulator microresonator," *Proceedings of the Conference on Lasers and Electro-Optics JTh5A.9*, 2015.

[64] S. A. Campbell, *The Science and Engineering of Microelectronic Fabrication*. Oxford University Press, 3rd ed., 2008.

[65] G. K. Celler and S. Cristoloveanu, "Frontiers of silicon-on-insulator," *Journal of Applied Physics*, vol. 93, no. 9, pp. 4955–4978, 2003.

[66] E. Dulkeith, Y. a. Vlasov, X. Chen, N. C. Panoiu, and R. M. Osgood, Jr., "Self-phase-modulation in submicron silicon-on-insulator photonic wires," *Optics Express*, vol. 14, no. 12, pp. 5524–5534, 2006.

[67] A. C. Turner-Foster, M. A. Foster, J. S. Levy, C. B. Poitras, R. Salem, A. L. Gaeta, and M. Lipson, "Ultrashort free-carrier lifetime in low-loss silicon nanowaveguides," *Optics Express*, vol. 18, no. 4, pp. 3582–3591, 2010.

[68] F. Da Ros, D. Vukovic, A. Gajda, K. Dalgaard, L. Zimmermann, B. Tillack, M. Galili, K. Petermann, and C. Peucheret, "Phase regeneration of DPSK signals in a silicon waveguide with reverse-biased p-i-n junction," *Optics Express*, vol. 22, no. 5, pp. 5029–5036, 2014.

[69] B. Corcoran, C. Monat, C. Grillet, D. J. Moss, B. J. Eggleton, T. P. White, L. O'Faolain, and T. F. Krauss, "Green light emission in silicon through slow-light enhanced third-harmonic generation in photonic-crystal waveguides," *Nature Photonics*, vol. 3, no. 4, pp. 206–210, 2009.

[70] B. Kuyken, X. Liu, G. Roelkens, R. Baets, R. M. Osgood, Jr., and W. M. J. Green, "50 dB parametric on-chip gain in silicon photonic wires," *Optics Letters*, vol. 36, no. 22, pp. 4401–4403, 2011.

[71] M. a. Foster, A. C. Turner, J. E. Sharping, B. S. Schmidt, M. Lipson, and A. L. Gaeta, "Broad-band optical parametric gain on a silicon photonic chip," *Nature*, vol. 441, no. 7096, pp. 960–963, 2006.

[72] R. L. Espinola, J. I. Dadap, R. M. Osgood, Jr, S. J. McNab, and Y. A. Vlasov, "C-band wavelength conversion in silicon photonic wire waveguides," *Optics Express*, vol. 13, no. 11, pp. 4341–4349, 2005.

[73] A. C. Turner, M. A. Foster, A. L. Gaeta, and M. Lipson, "Ultra-low power parametric frequency conversion in a silicon microring resonator," *Optics Express*, vol. 16, no. 7, pp. 4881–4887, 2008.

[74] H. Fukuda, K. Yamada, T. Shoji, M. Takahashi, T. Tsuchizawa, T. Watanabe, J.-I. Takahashi, and S.-I. Itabashi, "Four-wave mixing in silicon wire waveguides," *Optics Express*, vol. 13, no. 12, pp. 4629–4637, 2005.

[75] W. Mathlouthi, H. Rong, and M. Paniccia, "Characterization of efficient wavelength conversion by four-wave mixing in sub-micron silicon waveguides," *Optics Express*, vol. 16, no. 21, pp. 16735–16745, 2008.

[76] Y.-H. Kuo, H. Rong, V. Sih, S. Xu, M. Paniccia, and O. Cohen, "Demonstration of wavelength conversion at 40 Gb/s data rate in silicon waveguides," *Optics Express*, vol. 14, no. 24, pp. 11721–11726, 2006.

[77] A. Harke, M. Krause, and J. Mueller, "Low-loss singlemode amorphous silicon waveguides," *Electronic Letters*, vol. 41, no. 25, pp. 41–42, 2005.

[78] B. Kuyken, H. Ji, S. Clemmen, S. K. Selvaraja, H. Hu, M. Pu, M. Galili, P. Jeppesen, G. Morthier, S. Massar, L. K. Oxenløwe, G. Roelkens, and R. Baets, "Nonlinear properties of and nonlinear processing in hydrogenated amorphous silicon waveguides," *Optics Express*, vol. 19, no. 26, pp. B146–B153, 2011.

[79] Y. Shoji, T. Ogasawara, T. Kamei, Y. Sakakibara, S. Suda, K. Kintaka, H. Kawashima, M. Okano, T. Hasama, H. Ishikawa, and M. Mori, "Ultrafast nonlinear effects in hydrogenated amorphous silicon wire waveguide," *Optics Express*, vol. 18, no. 6, pp. 5668–5673, 2010.

[80] S. Suda, K. Tanizawa, Y. Sakakibara, T. Kamei, K. Nakanishi, E. Itoga, T. Ogasawara, R. Takei, H. Kawashima, S. Namiki, M. Mori, T. Hasama, and H. Ishikawa, "Pattern-effect-free all-optical wavelength conversion using a hydrogenated amorphous silicon waveguide with ultra-fast carrier decay," *Optics Letters*, vol. 37, no. 8, pp. 1382–1384, 2012.

[81] B. Kuyken, S. Clemmen, S. K. Selvaraja, W. Bogaerts, D. V. Thourhout, P. Emplit, S. Massar, G. Roelkens, and R. Baets, "On-chip parametric amplification with 26.5 dB gain at telecommunication wavelengths using CMOS-compatible hydrogenated amorphous silicon waveguides," *Optics Letters*, vol. 36, no. 4, pp. 552–554, 2011.

[82] C. Grillet, L. Carletti, C. Monat, P. Grosse, B. Ben Bakir, S. Menezo, J. M. Fedeli, and D. J. Moss, "Amorphous silicon nanowires combining

high nonlinearity, FOM and optical stability," *Optics Express*, vol. 20, no. 20, pp. 22609–22615, 2012.

[83] K. Narayanan and S. F. Preble, "Optical nonlinearities in hydrogenated-amorphous silicon waveguides," *Optics Express*, vol. 18, no. 9, pp. 8998–9005, 2010.

[84] K.-Y. Wang and A. C. Foster, "Ultralow power continuous-wave frequency conversion in hydrogenated amorphous silicon waveguides," *Optics Letters*, vol. 37, no. 8, pp. 1331–1333, 2012.

[85] J. Matres, G. C. Ballesteros, P. Gautier, J.-M. Fédéli, J. Martí, and C. J. Oton, "High nonlinear figure-of-merit amorphous silicon waveguides," *Optics Express*, vol. 21, no. 4, pp. 3932–3940, 2013.

[86] J. Safioui, F. Leo, B. Kuyken, S.-P. Gorza, S. K. Selvaraja, R. Baets, P. Emplit, G. Roelkens, and S. Massar, "Supercontinuum generation in hydrogenated amorphous silicon waveguides at telecommunication wavelengths," *Optics Express*, vol. 22, no. 3, pp. 3089–3097, 2014.

[87] U. D. Dave, S. Uvin, B. Kuyken, S. Selvaraja, F. Leo, and G. Roelkens, "Telecom to mid-infrared spanning supercontinuum generation in hydrogenated amorphous silicon waveguides using a Thulium doped fiber laser pump source," *Optics Express*, vol. 21, no. 26, pp. 32032–32039, 2013.

[88] D. T. Spencer, J. F. Bauters, M. J. R. Heck, and J. E. Bowers, "Integrated waveguide coupled Si_3N_4 in the ultrahigh-Q regime," *Optica*, vol. 1, no. 3, pp. 153–157, 2014.

[89] A. Gondarenko, J. S. Levy, and M. Lipson, "High confinement micron-scale silicon nitride high Q ring resonator," *Optics Express*, vol. 17, no. 14, pp. 11366–11370, 2009.

[90] J. S. Levy, A. Gondarenko, M. A. Foster, A. C. Turner-Foster, A. L. Gaeta, and M. Lipson, "CMOS-compatible multiple-wavelength oscillator for on-chip optical interconnects," *Nature Photonics*, vol. 4, no. 1, pp. 37–40, 2010.

[91] E. van de Ven, I.-W. Connick, and A. S. Harrus, "Advantages of dual frequency PECVD for deposition of ILD and passivation films," *International IEEE Conference TH-0325*, pp. 194–201, 1990.

[92] Y. Xuan, Y. Liu, L. T. Varghese, A. J. Metcalf, X. Xue, P.-H. Wang, K. Han, J. A. Jaramillo-Villegas, A. Al Noman, C. Wang, S. Kim, M. Teng, Y. J. Lee, B. Niu, L. Fan, J. Wang, D. E. Leaird, A. M. Weiner, and M. Qi, "High-Q silicon nitride microresonators exhibiting low-power frequency comb initiation," *Optica*, vol. 3, no. 11, pp. 1171–1180, 2016.

[93] J. P. Epping, M. Hoekman, R. Mateman, A. Leinse, R. G. Heideman, A. van Rees, P. J. van der Slot, C. J. Lee, and K.-J. Boller, "High confinement, high yield Si_3N_4 waveguides for nonlinear optical applications," *Optics Express*, vol. 23, no. 2, pp. 642–648, 2015.

[94] M. H. P. Pfeiffer, A. Kordts, V. Brasch, M. Zervas, M. Geiselmann, J. D. Jost, and T. J. Kippenberg, "Photonic Damascene process for integrated high-Q microresonator based nonlinear photonics," *Optica*, vol. 3, no. 1, pp. 20–25, 2016.

[95] R. Halir, Y. Okawachi, J. S. Levy, M. A. Foster, M. Lipson, and A. L. Gaeta, "Ultrabroadband supercontinuum generation in a CMOS-compatible platform," *Optics Letters*, vol. 37, no. 10, pp. 1685–1687, 2012.

[96] J. S. Levy, M. A. Foster, A. L. Gaeta, and M. Lipson, "Harmonic generation in silicon nitride ring resonators," *Optics Express*, vol. 19, no. 12, pp. 11415–11421, 2011.

[97] F. Ferdous, H. Miao, D. E. Leaird, K. Srinivasan, J. Wang, L. Chen, L. T. Varghese, and A. M. Weiner, "Spectral line-by-line pulse shaping of an on-chip microresonator frequency comb," *Nature Photonics*, vol. 5, no. 12, pp. 770–776, 2011.

[98] A. R. Johnson, Y. Okawachi, J. S. Levy, J. Cardenas, K. Saha, M. Lipson, and A. L. Gaeta, "Chip-based frequency combs with sub-100 GHz repetition rates," *Optics Letters*, vol. 37, no. 5, pp. 875–877, 2012.

[99] T. Herr, K. Hartinger, J. Riemensberger, C. Y. Wang, E. Gavartin, R. Holzwarth, M. L. Gorodetsky, and T. J. Kippenberg, "Universal formation dynamics and noise of Kerr-frequency combs in microresonators," *Nature Photonics*, vol. 6, pp. 480–487, jun 2012.

[100] Q. Li, T. C. Briles, D. A. Westly, T. E. Drake, J. R. Stone, B. R. Ilic, S. A. Diddams, S. B. Papp, and K. Srinivasan, "Stably accessing octave-spanning microresonator frequency combs in the soliton regime," vol. 4, no. 2, pp. 16–18, 2016.

[101] H. T. Philipp, K. N. Andersen, W. Svendsen, and H. Ou, "Amorphous silicon rich silicon nitride optical waveguides for high density integrated optics," *Electronics Letters*, vol. 40, no. 7, 2004.

[102] S. Habermehl, "Stress relaxation in Si-rich silicon nitride thin films," *Journal of Applied Physics*, vol. 83, no. 9, pp. 4672–4677, 1998.

[103] C. Lacava, S. Stankovic, A. Z. Khokhar, T. D. Bucio, F. Gardes, G. T. Reed, D. J. Richardson, and P. Petropoulos, "Si-rich silicon nitride for nonlinear signal processing applications," *Scientific Reports*, vol. 7, no. 22, pp. 1–13, 2017.

[104] K. J. A. Ooi, D. K. T. Ng, T. Wang, A. K. L. Chee, S. K. Ng, Q. Wang, L. K. Ang, A. M. Agarwal, L. C. Kimerling, and D. T. H. Tan, "Pushing the limits of CMOS optical parametric amplifiers with USRN:Si_7N_3 above the two-photon absorption edge," *Nature Communications*, vol. 8, no. 13878, pp. 1–10, 2017.

[105] D. Duchesne, M. Peccianti, M. R. E. Lamont, M. Ferrera, L. Razzari, F. Légaré, R. Morandotti, S. Chu, B. E. Little, and D. J. Moss, "Supercontinuum generation in a high index doped silica glass spiral waveguide," *Optics Express*, vol. 18, no. 2, pp. 923–930, 2010.

[106] A. Pasquazi, M. Peccianti, Y. Park, B. E. Little, S. T. Chu, R. Morandotti, J. Azaña, and D. J. Moss, "Sub-picosecond phase-sensitive optical pulse characterization on a chip," *Nature Photonics*, vol. 5, no. 10, pp. 618–623, 2011.

[107] A. Pasquazi, Y. Park, J. Azaña, F. Légaré, R. Morandotti, B. E. Little, S. T. Chu, and D. J. Moss, "Efficient wavelength conversion and net parametric gain via four wave mixing in a high index doped silica waveguide," *Optics Express*, vol. 18, no. 8, pp. 7634–7641, 2010.

[108] A. Pasquazi, R. Ahmad, M. Rochette, M. Lamont, B. E. Little, S. T. Chu, R. Morandotti, and D. J. Moss, "All-optical wavelength conversion in an integrated ring resonator," *Optics Express*, vol. 18, no. 4, pp. 3858–3863, 2010.

[109] M. Peccianti, A. Pasquazi, Y. Park, B. Little, S. Chu, D. Moss, and R. Morandotti, "Demonstration of a stable ultrafast laser based on a nonlinear microcavity," *Nature Communications*, vol. 3, no. 765, pp. 1–6, 2012.

[110] L. Razzari, D. Duchesne, M. Ferrera, R. Morandotti, S. Chu, B. E. Little, and D. J. Moss, "CMOS-compatible integrated optical hyper- parametric oscillator," *Nature Photonics*, vol. 4, no. 1, pp. 41–45, 2010.

[111] C. Lundström, R. Malik, L. Grüner-Nielsen, B. Corcoran, S. L. I. Olsson, M. Karlsson, and P. A. Andrekson, "Fiber optic parametric amplifier with 10-dB net gain without pump dithering," *IEEE Photonics Technology Letters*, vol. 25, no. 3, pp. 234–237, 2013.

[112] S. J. Madden, D.-Y. Choi, D. A. Bulla, A. V. Rode, B. Luther-Davies, V. G. Ta'eed, M. D. Pelusi, and B. J. Eggleton, "Long, low loss etched As(2)S(3) chalcogenide waveguides for all-optical signal regeneration," *Optics Express*, vol. 15, no. 22, pp. 14414–14421, 2007.

[113] M.-C. Tien, J. F. Bauters, M. J. R. Heck, D. J. Blumenthal, and J. E. Bowers, "Ultra-low loss Si_3N_4 waveguides with low nonlinearity and high power handling capability," *Optics Express*, vol. 18, pp. 23562–23568, nov 2010.

[114] L. Tsybeskov, D. J. Lockwood, and M. Ichikawa, "Silicon photonics: CMOS going optical," *Proceedings of the IEEE*, vol. 97, no. 7, pp. 1161–1165, 2009.

[115] W. Bogaerts, R. Baets, P. Dumon, V. Wiaux, S. Beckx, D. Taillaert, B. Luyssaert, J. Van Campenhout, P. Bienstman, and D. Van Thourhout, "Nanophotonic waveguides in silicon-on-insulator fabricated with CMOS technology," *Journal of Lightwave Technology*, vol. 23, no. 1, pp. 401–412, 2005.

[116] M. Paniccia and N. Photonics, "Integrating silicon photonics," *Nature Photonics*, vol. 4, no. 8, pp. 498–499, 2010.

[117] P. Dumon, W. Bogaerts, R. Baets, J.-M. Fedeli, and L. Fulbert, "Towards foundry approach for silicon photonics: silicon photonics platform ePIXfab," *Electronics Letters*, vol. 45, no. 12, pp. 581–582, 2009.

[118] G. E. Jellison Jr and F. A. Modine, "Parameterization of the optical functions of amorphous materials in the interband region," *Applied Physics Letters*, vol. 69, no. 3, pp. 371–373, 1996.

[119] N. Daldosso, M. Melchiorri, F. Riboli, M. Girardini, G. Pucker, M. Crivellari, P. Bellutti, A. Lui, and L. Pavesi, "Comparison among various Si_3N_4 waveguide geometries grown within a CMOS fabrication pilot line," *Journal of Lightwave Technology*, vol. 22, no. 7, pp. 1734–1740, 2004.

[120] X.-J. Liu, J.-J. Zhang, X.-W. Sun, Y.-B. Pan, L.-P. Huang, and C.-Y. Jin, "Growth and properties of silicon nitride films prepared by low pressure chemical vapor deposition using trichlorosilane and ammonia," *Thin Solid Films*, vol. 460, pp. 72–77, 2004.

[121] C.-K. Chung, M.-Q. Tsai, P.-H. Tsai, and C. Lee, "Fabrication and characterization of amorphous Si films by PECVD for MEMS," *Journal of Micromechanics and Microengineering*, vol. 15, pp. 136–142, 2005.

[122] J. M. Chavez Boggio, D. Bodenmüller, T. Fremberg, R. Haynes, M. M. Roth, R. Eisermann, M. Lisker, L. Zimmermann, and M. Böhm, "Dispersion engineered silicon nitride waveguides by geometrical and refractive-index optimization," *Journal of the Optical Society of America B*, vol. 31, no. 11, pp. 2846–2857, 2014.

[123] M. Belyansky, M. Chace, O. Gluschenkov, J. Kempisty, N. Klymko, A. Madan, A. Mallikarjunan, S. Molis, Y. Ronsheim, D. Yang, and Y. Li, "Methods of producing plasma enhanced chemical vapor deposition silicon nitride thin films with high compressive and tensile stress," *Journal of Vacuum Science and Technology A*, vol. 26, no. 3, pp. 517–521, 2008.

[124] A. Gorin, A. Jaouad, E. Grondin, V. Aimez, and P. Charette, "Fabrication of silicon nitride waveguides for visible-light using PECVD: a study of the effect of plasma frequency on optical properties," *Optics Express*, vol. 16, no. 18, pp. 13509–13516, 2008.

Appendix A

Clean room processes

In this appendix, we describe the clear room recipes used to manufacture the optical waveguides presented in Paper B–F.

Recipe for optical waveguide fabrication

1. Growth of silicon dioxide in Centrotherm oxidation furnace

Silicon substrate	3-inch, p-doped/Boron, <100>
Temperature	1 100°C
Gas flow	O_2 5 l/min, H_2 8 l/min
Oxidation time	1 200 min
Thickness SiO_2	3 µm

2. Deposition of silicon nitride in Centrotherm LPCVD furnace

Si_3N_4 - DCS:NH_3 0.27	770°C, 250 mTorr, DCS 98.1 sccm, NH_3 360 sccm growth rate center 4.02 nm/min, growth rate edge 4.24 nm/min
Si_xN_y - DCS:NH_3 4	770°C, 200 mTorr, DCS 240 sccm, NH_3 60 sccm growth rate center 4.06 nm/min, growth rate edge 4.21 nm/min
Si_xN_y - DCS:NH_3 8	770°C, 200 mTorr, DCS 126 sccm, NH_3 15.8 sccm growth rate center 2.93 nm/min, growth rate edge 3.11 nm/min
Si_xN_y - DCS:NH_3 12	770°C, 200 mTorr, DCS 240 sccm, NH_3 20 sccm growth rate center 3.07 nm/min, growth rate edge 3.23 nm/min
Si_xN_y - DCS:NH_3 16.67	770°C, 200 mTorr, DCS 250 sccm, NH_3 15 sccm growth rate center 2.43 nm/min, growth rate edge 2.55 nm/min

3. Photolithography to define etchmask in mask aligner Sucss MJB3 DUV

Wafer cleaning	Rinse in Acetone, Isopropanol, Water and blowdry with N_2
Adhesion promotion	HDMS primer
Spin photoresist UV60-0.75	3 500 rpm, 45 s, 1 000 ms acceleration/deceleration
Softbake on hotplate	130°C, 4 min
Exposure settings	800 ms, DUV (200 − 260 nm wavelength), vacuum-mode
Post-exposure bake on hotplate	130°C, 1 min
Development in MF-CD-26	45 sec (rinse in water and blowdry with N_2)
Descum in oxygen plasma	150 W, 2 min
Hardbake in oven	130°C, 15 min

4. Reactive-ion etching of silicon nitride in Oxford Plasmalab 100

RF Generator power	50 W
ICP power	150 W, 16.5 MHz
Pressure	95 mTorr
Gas flow	CHF_3 50 sccm, O_2 10 sccm
Etchrate	∼ 45 nm/min
Resist removal	Acetone 5 min, MR-rem 400 55°C 5 min + ultrasonic 5 min, Isopropanol 3 min, rinse in water and blowdry with N_2

5. Polymer removal in standard clean process (SC1 + SC2)

SC1 (H_2O_2+NH_3+H_2O)	80°C 10 min (rinse in water)
HF	1 min (rinse in water)
SC2 (H_2O_2+HCl+H_2O)	70°C 10 min (rinse in water and blowdry with N_2)

6. Deposition of silicon dioxide in STS PECVD chamber

Pressure	550 mTorr
Gas flow	SiH_4 400 sccm, N_2O 1 420 sccm
Deposition rate	44 nm/min

Recipe for crack barrier fabrication

1. Laser lithography to define crack barriers in Heidelberg Instruments DWL 2000

Wafer cleaning	Rinse in Acetone, Isopropanol, Water and blowdry with N_2
Adhesion promotion	HDMS primer
Spin photoresist S1813	3 500 rpm, 45 s, 1 000 ms acceleration/deceleration
Soft bake on hotplate	115°C, 2min
Exposure parameters	Focus offset 0, Intensity 100, Transmission 100
Development in MF319	60 sec (rinse in water and blowdry with N_2)

2. Etching of silicon dioxide in HF bath

Duration	37.5 min
Etch rate	80 nm/min

Recipe for annealing of silicon nitride

1. Annealing of silicon nitride film in Thermolyne M. 59340 furnace

Temperature	1 200°C
Gas flow	N_2 20 s.u.
Duration	3 h